Transverse Reinforcement Configurations in GFRP-Reinforced Concrete Columns: Experiments and Damage Mechanics-Based Modeling

Alireza Sadat Hosseini[1*] and Pedram Sadeghian[2]

[1] Research Assistant, Department of Civil and Resource Engineering, Dalhousie University, Canada
[2] Associate Professor and Canada Research Chair in Sustainable Infrastructure, Department of Civil and Resource Engineering, Dalhousie University, Canada
* Corresponding Author, email: asadat@dal.ca

ABSTRACT

The effects of transverse reinforcement configurations on the strength and deformability of concrete columns reinforced with glass fiber-reinforced polymer (GFRP) bars and ties were studied, with emphasis on post-peak performance. A new experimental method exposed columns without concrete cover to directly observe the failure modes of longitudinal and transverse GFRP bars. The experiments were supported by 3D finite element (FE) models using concrete damage plasticity (CDP) for concrete and the LaRC05 failure criteria for GFRP bars. The findings reveal that reducing the tie spacing from $12d_b$ to $6d_b$ (d_b is the longitudinal bar's nominal diameter) increased the deformability index from 0.25 to 0.8 and enhanced post-peak load retention from 0.001 µm/m to 0.011 µm/m. Increasing the tie overlap length from $20d_t$ to $28d_t$ (d_t is the tie's nominal diameter) improved confinement, delaying bar buckling and increasing second peak load by 17%. Additionally, using fasteners at $3d_t$ intervals on tie overlaps maintained tie integrity post-peak, ensuring more stable behavior. Large-scale tests from the literature were analyzed and categorized into three deformability classes based on axial load-displacement and stress-strain behavior. A deformability index, I_{AD}, was proposed, showing a linear relationship with the transverse reinforcement ratio, ρ_t, with a coefficient of determination (R^2) of 0.84. A comparative analysis of FEM approaches for modeling GFRP-RC columns further validated these findings.

DOI: https://doi.org/10.1016/j.jobe.2025.112368

Keywords: GFRP-Reinforced Concrete Column; Experiments; Finite Element Model (FEM); deformability; Tie configuration

NOMENCLATURE

A_t: cross-sectional area of tie
b: larger dimension of the column cross section
d: damage variable
d_{agg}: nominal maximum size of aggregate
d_b: nominal diameter of longitudinal bar
d_c: compressive damage variable
d_t: nominal diameter of transverse reinforcement, tensile damage variable
e: eccentricity
E_c: concrete elastic modulus
f_c': concrete ultimate strength
F_f^k: fiber kinking index
F_f^s: fiber splitting index
F_f^t: fiber tensile failure criterion
F_m^{cr}: matrix cracking index
f_t: concrete maximum tensile strength
G: non-associated potential flow function
G_f: fracture energy
G_{f0}: base fracture energy
I_{AD}: deformability index
K_c: ratio of the second stress invariant on the tensile meridian to that on the compressive meridian at initial yield
l_c: element characteristic length
L_u: bar specimen gauge length in compression/tension test
n: curve fitting number in stress-strain equation for concrete, number of tie cross-sections in a plain
p: hydrostatic pressure
$P_{max,2}$: axial second peak load of column
P_{max}: axial peak load of column
q: Mises equivalent effective stress
s: tie or hoop center-to-center spacing
S_L: in-plane shear strength
S_T: transverse shear strength
X_C: longitudinal compressive strength
X_T: longitudinal tensile strength
Y_C: transverse compressive strength
Y_T: transverse tensile strength
α: angle of the critical plane
α_0: angle of the critical plane under pure transverse compression δ_0: axial displacement at peak load
Δf: stress drop in stress-strain diagram
ΔP: load drop in load-displacement diagram
δ_u: axial displacement corresponding to 15% load drop
ε_c': strain of concrete corresponding to its ultimate strength
ε_0: axial strain at ultimate strength
ε_c: compressive strain in concrete
ε_{cu}: maximum usable compressive strain of concrete
ε^{el}: elastic strain
ε^{pl}: plastic strain
ε_s: strain in steel bars
ε_u: axial strain corresponding to 15% stress drop
η_L: material parameters associated with longitudinal shear stress interaction in the failure criterion
η_T: material parameters associated with transverse shear stress interaction in the failure criterion
μ: viscosity parameter
ν: Poisson's ratio
ρ: density
ρ_t: transverse reinforcement ratio (not volumetric)
σ_{22}: normal stress in the 2-direction (transverse direction)
σ_{33}: normal stress in the 3-direction
σ_{b0}: initial biaxial compressive yield stress
σ_{c0}: initial uniaxial compressive yield stress
σ_c: uniaxial compressive stress
σ_{max}: maximum principal effective stress
σ_N: normal stress acting on the fracture plane
σ_t: uniaxial tensile stress
τ_{12}: shear stress in the 1-2 plane
τ_{13}: shear stress in the 1-3 plane
τ_{23}: shear stress in the 2-3 plane
τ_L: shear stress in the longitudinal direction on the fracture plane
τ_T: shear stress in the transverse direction on the fracture plane
ψ: concrete dilation angle

ABBREVIATIONS

CDP: Concrete Damage Plasticity
CFRP: Carbon Fiber Reinforced Polymer
DAMAGEC: concrete damage indicator
FE: Finite Element
FEM: Finite Element Model
LARCFKCRT: LaRC05 fiber kinking damage initiation criterion
LARCMCCRT: LaRC05 matrix cracking damage initiation criterion
LVDT: Linear Variable Differential Transformer

FRP: Fiber Reinforced Polymer
GFRP: Glass Fiber Reinforced Polymer
GFRP-RC: Glass Fiber-Reinforced Polymer-Reinforced Concrete
RC: Reinforced Concrete

1. INTRODUCTION

GFRP bars have gained significant attention as a non-corrosive and sustainable alternative to steel reinforcement. Similar to steel-RC columns, GFRP-RC columns use transverse reinforcement in the form of hoops or ties for circular and square columns, respectively, or continuous spirals (helices). Research in this field has largely focused on understanding the influence of key factors such as tie spacing or spiral pitch, the shape of ties in plan, and the size of transverse reinforcement bars, all of which are key to the structural performance and deformability of GFRP-RC columns.

Jawaheri Zadeh and Nanni [1] used the same buckling idea as the steel longitudinal bars for GFRP bars by limiting their strain to 0.003 and suggested a modification to the allowable tie spacing for steel bars in ACI 318-11 [2], recommending a maximum tie spacing of $12d_b$ for GFRP bars. De Luca et al. [3] suggested that tie spacing strongly influences failure modes without increasing peak capacity. After concrete cover splitting, the concrete core was partially confined by C-shaped GFRP ties, prompting development of closed GFRP ties. Elchalakani and Ma [4] investigated the axial capacity of rectangular GFRP-RC columns compared to steel counterparts. Under concentric load, columns achieve 93.5% of steel counterparts' average axial load capacity. GFRP columns exhibited a 3.2% average increase in load capacity compared to plain concrete, while steel columns achieved 15.8%. They concluded that despite potential measurement errors, GFRP may not significantly contribute to ultimate load capacity due to tie spacing causing local buckling of longitudinal bars. In Guérin et al. [5] experiments on full-scale square GFRP-RC columns, it was seen that using GFRP ties as transverse reinforcement prevented buckling and confined concrete core effectively, up to 12,000 με compressive strain. Based on further studies by Guérin et al. [6], utilizing half the maximum GFRP tie spacing mandated in the steel-RC code, ACI 318-14 [7], effectively prevented longitudinal reinforcement buckling. Tests on square GFRP-RC columns by Tobbi et al. [8] showed that well-confined specimens saw significant strength and ductility gains post-concrete spalling. GFRP transverse reinforcement substantially enhanced strength, toughness, and ductility, with tie configuration and spacing pivotal. In further investigation by Tobbi et al. [9], tie configuration and spacing showed the efficacy of GFRP as transverse reinforcement in augmenting the ductility, toughness, and strength of the confined core. Based on test results from square RC columns using GFRP and CFRP ties, Tobbi [10] observed that FRP ties significantly enhanced concrete deformability and strength. However, closed FRP ties showed superiority over C-shaped ties [11] in terms of confinement effectiveness. More recently, Salah-Eldin et al. [12] found that increasing tie complexity in the cross-section, while maintaining constant spacing along the length, enhanced deformability under eccentric loads. Elmesalami et al. [13] tested square GFRP-RC columns with tie spacing equal to the section side dimension. Their concentric tests showed a 10.5% increase in ultimate load capacity.

Afifi et al. [14] examined the behavior of circular CFRP-RC columns under compression. A smaller pitch and diameter of CFRP spirals exhibited improved ductility and confinement efficiency, leading to a more gradual failure progression compared to columns with larger, widely spaced spirals. Conversely, columns with large spiral spacing or small volumetric ratios demonstrate failure due to diagonal shear plane cutting through the reinforcement. In the study by Mohamed et al. [15], FRP spirals and hoops effectively confined the concrete core post-peak, with the latter attaining 1.3% and 2.2% higher strength, respectively, and an overlap length of

20dt in hoops prevented premature failure. Circular GFRP-RC columns with helices were tested by Karim et al. [16] and found that decreasing the pitch of GFRP helices enhances ductility capacity by approximately 1.5 times for columns with longitudinal bars and by around 2.2 times for columns without them. Hadi et al. [17] found that decreasing the pitch of GFRP helices from 60 to 30 mm enhanced the performance of circular GFRP-RC specimens, improving their ductility, bending moment resistance, and load-carrying capacity. Hadhood et al. [18] investigated full-scale circular CFRP-RC columns and found that CFRP spirals effectively provided lateral support to both compression and tension bars, confining the concrete core until and after the peak load, with spirals tensile strains exceeding 1%. Abdelazim et al. [19] tested circular columns with spirals and observed that reducing the spiral pitch from $5d_b$ to $2.5d_b$ halved the load drop after peak load in concentric tests. Elchalakani et al. [20] tested circular columns with spirals and noted that specimens with a $4d_b$ spiral pitch exhibited a second peak load close to the first peak in the load-displacement diagram. Increasing the pitch to $8d_b$ maintained the load after the initial drop but prevented the development of a second peak, while further increasing it to $12d_b$ led to a sudden load drop after peak load. Hadi et al. [21] studied circular geopolymer concrete columns and found that reducing the spiral pitch from 0.47 to 0.25 times the section diameter increased load capacity by 10% and improved deformability by 15%.

The design of transverse reinforcement for GFRP-RC columns must account for the brittle failure characteristics of GFRP, making it fundamentally different from that of conventional steel-RC columns. Columns with large tie spacing, such as $12d_b$, have exhibited brittle failure, necessitating further investigation to determine appropriate tie spacing that ensures the required ductility. ACI CODE-440.11 [22] recommends that the clear spacing between ties should be at least $(4/3)d_{agg}$, and the center-to-center spacing should not exceed the lesser of $12d_b$,

$24d_t$, or the smallest dimension of the member. While these recommendations are more conservative than the minimum requirements of ACI 318-19 [23], they ensure compliance with minimum requirements for safe construction. However, additional adjustments to tie spacing and configuration may be necessary for applications requiring greater deformability. Furthermore, the manufacturing method of the ties—whether C-shaped or cut from continuous spirals—also influences performance, particularly with respect to overlap. ACI CODE-440.11-22 [22] specifies a $20d_t$ overlap when only 90^{o} hooks are available. However, the effectiveness of this overlap depends on the tie shape and how the overlaps are fastened, for example, using zip ties at specified intervals.

Despite significant research on GFRP-RC columns, critical aspects such as tie overlap length in square columns and the effects of fastener quality and spacing remain underexplored. This study systematically investigates the influence of tie spacing, overlap length, tie shape, and fastening intervals on the strength, ductility, and post-peak behavior of GFRP-RC columns. A novel experimental approach was introduced, where small-scale columns were tested without a concrete cover, enabling direct observation of tie and longitudinal reinforcement behavior, particularly in the post-peak region. The experimental findings were supplemented by advanced 3D finite element models (FEMs) incorporating concrete damage plasticity (CDP) and the LaRC05 failure criteria for GFRP reinforcement, ensuring a comprehensive assessment of structural behavior. To bridge the gap between experimental results and design applications, a deformability index was proposed based on axial load-deformation behavior, informed by both numerical simulations and a critical review of existing large-scale test data from the literature. The findings provide insights for improving design provisions and guiding future research on the optimization of GFRP-RC column detailing for enhanced structural performance.

2. EXPERIMENTS

2.1. Materials Characteristics

The concrete mix was made with a d_{agg}=12.5 mm, achieving a compressive strength of 42.0 ± 0.8 MPa at the time of testing, as determined by standard cylinder tests. #5 sand-coated GFRP bars (d_b = 15.9 mm) were utilized as longitudinal reinforcement, while #3 GFRP square ties (d_t = 9.5 mm) served as transverse reinforcement. Figure 1 shows the reinforcing materials used in this study.

To verify the tensile properties provided by the manufacturer, five tensile specimens of the longitudinal bars were prepared and tested according to ASTM D7205M [24]. The tensile tests revealed an average tensile strength of 1020 MPa, with a standard deviation of 25 MPa, closely matching the manufacturer's values (1019±25.9 MPa). The average ultimate tensile strain was 0.021±0.0005 and the average tensile elastic modulus was measured at 53,805±107 MPa. For #3 ties, the manufacturer provided a tensile strength of 460 MPa and an elastic modulus of 50,000 MPa.

Using a recently developed fixture [25], the compressive material properties (strength and modulus) of #5 bars were measured for three different L_u/d_b ratios of 2, 4, and 6. The average compressive strengths were 952±66 MPa, 873±61 MPa, and 703±105 MPa for the three L_u/d_b ratios, respectively. The average ultimate compressive strains were 0.018±0.002, 0.014±0.002, and 0.012±0.002, respectively. For compressive elastic modulus, tests on different L_u/d_b ratios of 2, 4, and 6 resulted in 50000, 50700, and 49500 MPa which are very close to the tensile modulus. It should be highlighted that there is no ASTM standard test method to obtain the compressive properties of FRP bars and the test fixture used in this study was developed based on previous research in the field [26], [27], [28], [29], [30].

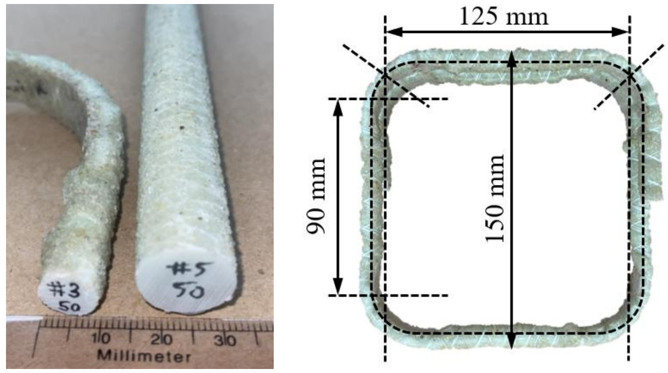

Figure 1 – GFRP bar and tie sample used in the experiments

2.2. Specimens Preparation

According to ACI CODE-440.11-22 [22] the spacing of GFRP ties must adhere to specific limits, including $12d_b$, $24d_t$, or the smallest dimension of the column. These specifications were influenced by the findings of Jawaheri Zadeh and Nanni [1], whose study utilized a simplified model assuming longitudinal bars function solely as compressive members supported by ties, excluding considerations for lateral support from concrete cover due to potential cover loss during failure. Their proposal aimed to harmonize the criteria for GFRP bars with those for steel bars. While steel typically experiences buckling post-yielding at $\varepsilon_s \approx 0.002$, GFRP bars should avoid buckling before concrete crushing at ε_{cu}=0.003. Consequently, this led to the establishment of stricter criteria in ACI-CODE440.11-22 [22] compared to those in ACI 318-19 [23].

Considering the negligible effect of cover on lateral support, a group of columns with a length-to-width ratio of 2 were constructed without concrete cover to investigate the pure effect of ties in laterally reinforcing longitudinal bars. A specialized formwork, depicted in Figure 2, was utilized to fabricate these coverless concrete columns.

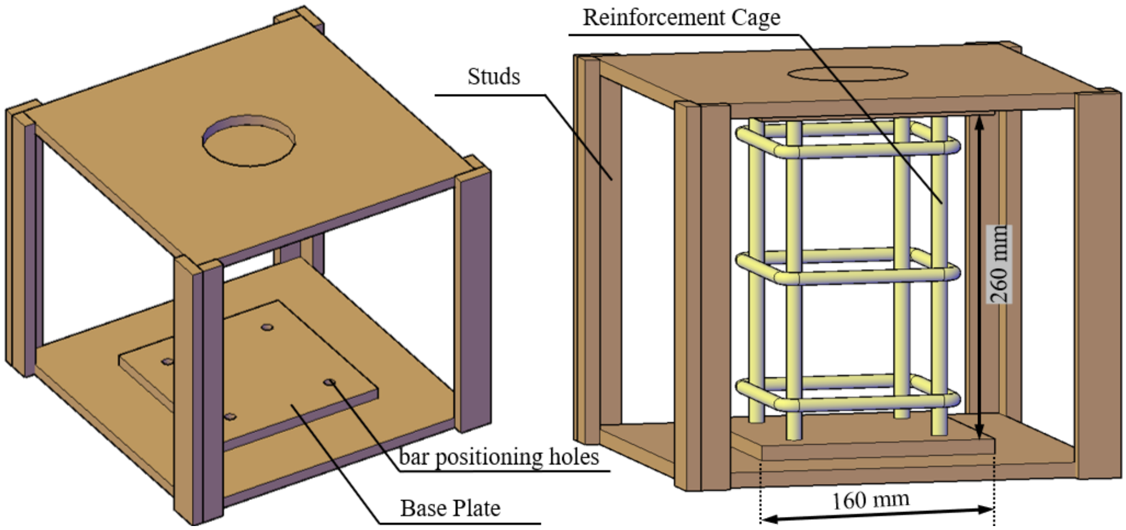

Figure 2 – Customized formwork for fabricating GFRP-reinforced columns devoid of concrete cover

A total of seven concrete columns were fabricated and tested under compressive load: three plain columns and four with exposed bars and ties, each having a square cross-section and a length of 260 mm. According to Table 1, the IDs for the reinforced columns follow the format "G-Sx-Ty." In this labeling system, "G" denotes GFRP reinforcement, "S" indicates spacing, "x" specifies the spacing in mm, and "T" stands for tie with "y" representing the tie type (1 or 2 based on the overlapping configuration). For instance, "R-S200-T20-1" refers to a GFRP-reinforced concrete column with tie configuration 1 and a tie spacing of 200 mm. Additionally, a plain concrete column with the ID "PC" is included in the table for comparison purposes.

The column fabrication process is illustrated in Figure 3. Using the specialized formwork depicted in Figure 2, GFRP #5 bars were cut to a length of 285 mm. Of this, 260 mm constituted the clear spacing between the top and bottom plywood plates (Figure 2), corresponding to the overall length of the column after concreting. Additional lengths were inserted into the plywood to secure the bars during concreting (Figure 3a). Next, self-adhesive film was wrapped around the bars to form the core of the column and provide a smooth surface for the concrete finish (Figure 3b). The ties were then attached to the longitudinal bars as shown in Figure 3c. This involved temporarily removing the top plywood, placing the ties around the bars, refitting the top plywood to keep the bars straight, and fixing the ties in place using zip ties. The specimens were wrapped with strong tape (Figure 3d) to ensure they held the concrete without deformation and bulging. Concrete was then prepared and poured into the formwork through a hole in the top plywood. The concrete was tamped and vibrated to compact it and reduce air pockets and voids. Three cylinders were prepared concurrently with the same batch of concrete for compression tests. The concrete remained in the formwork for seven days before the form, tapes, and self-adhesive film were removed. The columns and cylinders were then cured for 28 days in a suitable environment. When the specimens were removed from the formwork, both the top and bottom ends were wrapped with 30 mm wide CFRP to prevent local premature damage to the concrete. Before wrapping, the concrete surfaces were thoroughly cleaned as part of the surface preparation process.

Table 1 – Test matrix

Number	Specimen ID	Number of longitudinal bars	Tie spacing (mm)	Tie overlap length	Tie overlap configuration
1	PC	0	_	_	_
2	R-S100-T20-1	4	100 (≈6d_b*)	20d_t**	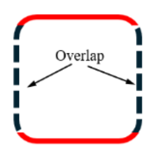
3	R-S100-T20-2	4	100 (≈6d_b*)	20d_t	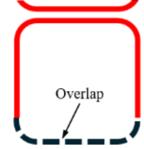
4	R-S100-T28-1	4	100 (≈6d_b*)	28d_t	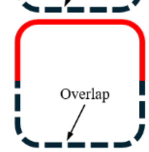
5	R-S200-T28-1	4	200 (≈12d_b*)	28d_t	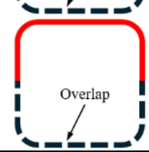

* d_b: Longitudinal bar nominal diameter
** d_t: Transverse reinforcement (tie) nominal diameter

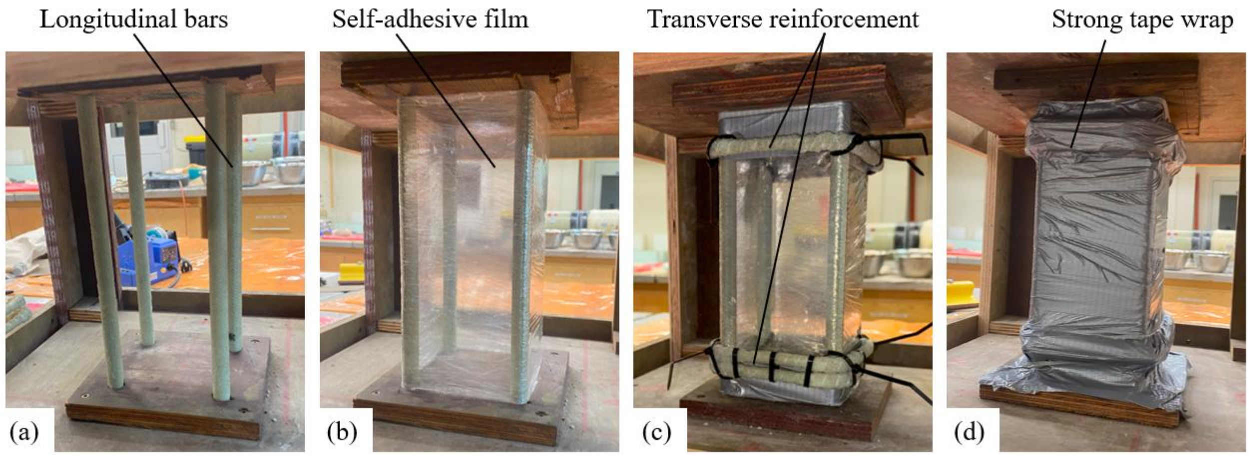

Figure 3 – Fabrication process of GFRP-reinforced columns without concrete cover (sample pictures from R-S200-T28-1)

2.3. Test Method

To ensure a smooth and uniform surface finish at the ends of the column specimens, the top and bottom surfaces were prepared with special attention due to the smooth surfaces resulting from the formwork. Initially, the concrete finish at these ends was inherently smooth; however, to mitigate any local failures caused by surface irregularities, the surfaces were lightly ground.

To facilitate accurate load application and prevent premature failure at the bar ends, two one-inch-thick square (200×200 mm) steel plates were used at both the top and bottom of the specimens. These plates had holes drilled in them according to the pattern of the longitudinal bars, allowing the extra length of the bars, which had been embedded in the formwork during concreting, to be inserted. The steel plates served a dual purpose: providing smooth end surfaces for load application and ensuring the bars resembled their continuity in the column, thereby reducing local effects at the column ends.

The specimens were tested under axial compressive load using a 2 MN universal testing machine. Displacement-controlled loading was applied at a constant rate of 1.0 mm per minute. Data acquisition was conducted at intervals of 0.1 seconds, capturing key measurements including the vertical displacement of the column and the applied load. Using two strain gauges affixed to the outer surface of the longitudinal bars the strain measurement was conducted. Additionally, two linear variable differential transformers (LVDTs) were installed at the mid-height of the column to record lateral displacements. The specimens and the test instrumentation are presented in Figure 4.

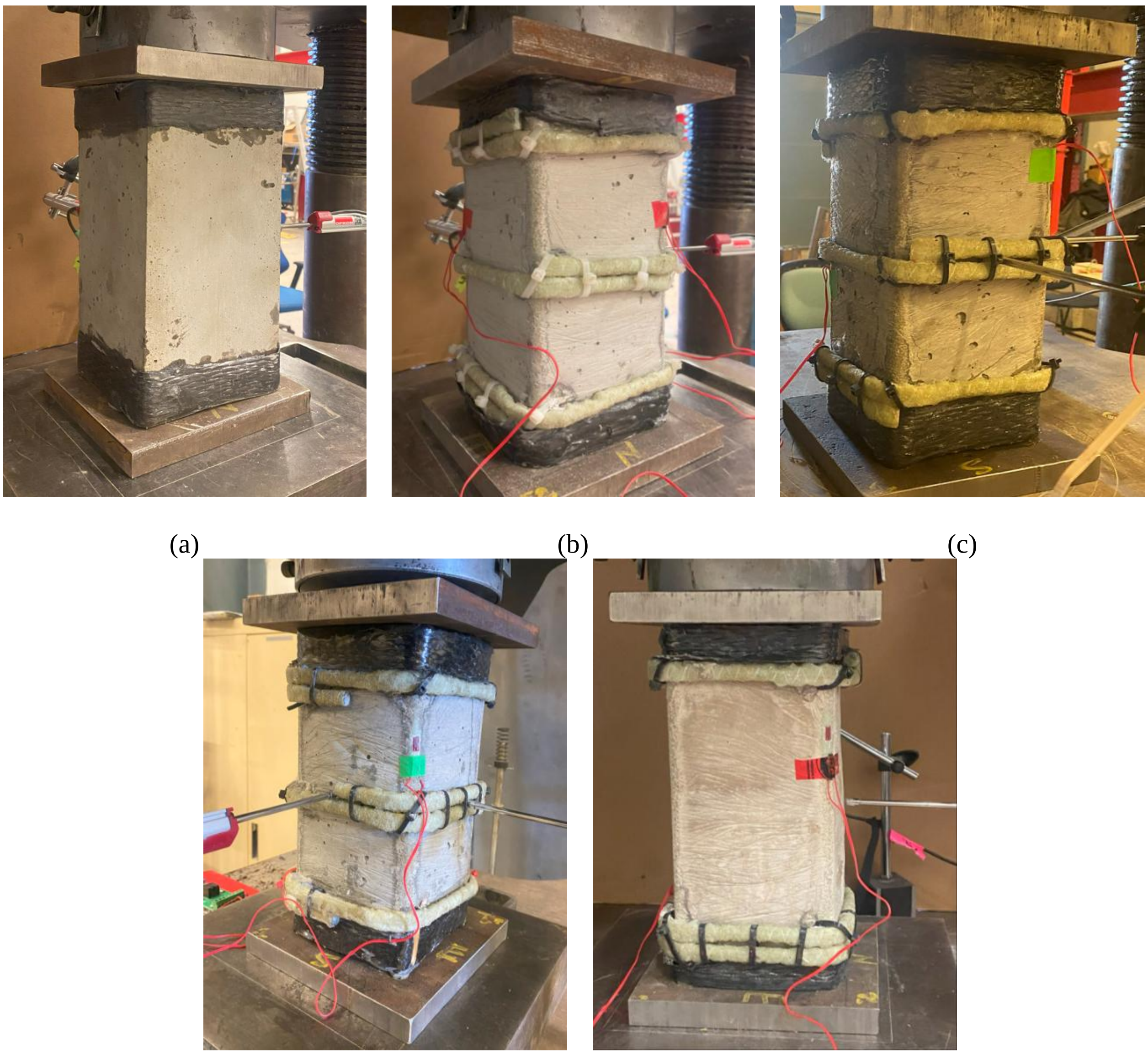

(a) (b) (c)

(d) (e)

Figure 4 – Test setup for GFRP-reinforced columns without concrete cover: a) PC, b) R-S100-T20-1, c) R-S100-T20-2, d) R-S100-T28-1, and e) R-S200-T28-1

3. NUMERICAL ANALYSIS

This section presents the FE analysis conducted using 3D modeling techniques in ABAQUS [31]. The following subsections describe the material properties, geometric configurations, boundary conditions, and analysis methods used in the simulations.

3.1. Material Properties

3.1.1. GFRP Bars

Table 2 presents the calibrated mechanical properties of the reinforcement used in the analysis. Both bar sizes have a guaranteed tensile and compressive modulus of 50 GPa, indicating similar stiffness in tension and compression. The manufacturer specifies a tensile strength of 460 MPa for #3 bent bars and 1000 MPa for #5 bars. After calibration, the tensile strength of #5 bars was adjusted to 1010 MPa, within the tested range. The compressive strength of #3 bars was estimated as 355 MPa based on the compressive-to-tensile strength ratio of #5 bars, while the calibrated compressive strength was set at 780 MPa, aligning with test results across various length-to-diameter ratios.

Table 2 – Calibrated mechanical properties of GFRP bars used in FE models

Bar size	Nominal diameter (mm)	Tensile modulus* (GPa)	Compressive Modulus* (GPa)	Tensile Strength** (MPa)	Compressive Strength** (MPa)
#3	d_t = 9.5	50	50	460	355
#5	d_b = 15.9	50	50	1010	780

* The elastic modulus in tension and compression is set to an equal guaranteed value for simplicity.
** The strength values are the calibrated values in the FE models within the range of experiments results.

Failure in three-dimensional fiber-reinforced composites can be predicted using the LaRC05 criterion, as outlined in the work by Pinho et al. [32]. This criterion, which is applicable to unidirectional solid composites [31], addresses four primary damage initiation mechanisms:

matrix cracking, tensile failure of fiber, fiber failure under compression in the form of fiber kinking, and fiber splitting. Pinho et al. [32] introduced a modified version of the Mohr-Coulomb failure criterion tailored for matrix-dominated failures in unidirectional composites. This adaptation directly incorporates the fracture angle to predict the consequences of failure more accurately. The matrix cracking index is defined as:

$$(F_m^{cr})^2 = \left(\frac{\langle\sigma_N\rangle_+}{Y_T}\right)^2 + \left(\frac{\tau_L}{S_L - \eta_L\sigma_N}\right)^2 + \left(\frac{\tau_T}{S_T - \eta_T\sigma_N}\right)^2 \tag{1}$$

Where, $\langle\sigma_N\rangle_+ = max\{\sigma_N, 0\}$, and $F_m^{cr} \geq 1$ indicates the failure condition, and stress terms are defined as:

$$\sigma_N = \sigma_{22}cos^2\alpha + \sigma_{33}sin^2\alpha + \sigma_{33}sin(2\alpha)$$

$$\tau_T = \frac{1}{2}(\sigma_{33} - \sigma_{22})sin(2\alpha) + \tau_{23}cos(2\alpha) \tag{2}$$

$$\tau_L = \tau_{12}cos\alpha + \tau_{13}sin\alpha$$

Eq. (1) applies to both tensile and compressive matrix cracking. The final term in this equation represents the positive normal traction that causes the matrix crack to open. In Eq. (2), α denotes the angle of the critical plane where F_m^{cr} reaches its maximum value. Particularly under pure transverse compression, α is shown as α_0, typically ranging between 51° and 55° for glass or carbon composites (for example for E-glass/DY063 epoxy, α_0=53° [33]). The coefficients η_L and η_T are defined to decrease the respective shear strengths under tensile normal traction and increase the respective shear strengths under compressive normal traction:

$$\eta_L = \frac{S_L cos(2\alpha_0)}{Y_C cos^2\alpha_0} \tag{3}$$

$$\eta_T = -\frac{1}{tan(2\alpha_0)} \tag{4}$$

η_L for glass-epoxy composites can be in a range of 0.08 to 0.2 [32]. The other failure criterion is fiber tensile failure corresponding to maximum positive axial stress along the fibers:

$$F_f^t = \frac{\sigma_{11}}{X_T} \tag{5}$$

Under compressive loading, kink bands are observed when compressive failure happens. This can be a result of fibers micro buckling or localized failures in matrix adjacent to misaligned fibers. This misalignment results in fiber kinking when shear-dominated matrix failure occurs under significant compressive stress, σ_{11}, having larger absolute values as the longitudinal compressive strength, X_C ($\sigma_{11} \leq -\frac{X_C}{2}$). If compressive stress is not significant ($-\frac{X_C}{2} \leq \sigma_{11} \leq 0$), fiber splitting happens but kinking does not occur:

$$\left(F_f^k\right)^2 = \left(\frac{\langle\sigma_2^m\rangle_+}{Y_T}\right)^2 + \left(\frac{\tau_{12}^m}{S_L - \eta_L\sigma_2^m}\right)^2 + \left(\frac{\tau_{23}^m}{S_T - \eta_T\sigma_2^m}\right)^2 \tag{6}$$

$$\left(F_f^s\right)^2 = \left(\frac{\langle\sigma_2^m\rangle_+}{Y_T}\right)^2 + \left(\frac{\tau_{12}^m}{S_L - \eta_L\sigma_2^m}\right)^2 + \left(\frac{\tau_{23}^m}{S_T - \eta_T\sigma_2^m}\right)^2 \tag{7}$$

In the fiber-misalignment frame, the stresses can be found using:

$$\begin{aligned}
\sigma_2^m &= \sigma_{11}sin^2\varphi + \sigma_{22}^{\psi}cos^2\varphi - 2\tau_{12}^{\psi}sin\varphi cos\varphi \\
\tau_{12}^m &= \tau_{12}^{\psi}cos^2\varphi - \tau_{12}^{\psi}sin^2\varphi + \left(\sigma_{22}^{\psi} - \sigma_{11}\right)sin\varphi cos\varphi \\
\tau_{23}^m &= \tau_{23}^{\psi}cos\varphi - \tau_{13}^{\psi}sin\varphi
\end{aligned} \tag{8}$$

Wherein the terms σ_{ij}^{ψ} and τ_{ij}^{ψ} stand for stresses in the fiber kinking plane.

$$\begin{aligned}
\sigma_{22}^{\psi} &= \sigma_{22}cos^2\psi + \sigma_{33}sin^2\psi + 2\tau_{23}sin\psi cos\psi \\
\tau_{12}^{\psi} &= \tau_{12}cos\psi + \tau_{13}sin\psi \\
\tau_{13}^{\psi} &= \tau_{13}cos\psi - \tau_{12}sin\psi \\
\tau_{23}^{\psi} &= \tau_{23}cos2\psi - (\sigma_{22} - \sigma_{33})sin\psi cos\psi
\end{aligned} \tag{9}$$

When calculating failure in the FE model, the sign of σ_{11} is checked first. If σ_{11} is positive, the tension failure criterion is applied. If σ_{11} is negative, the compressive failure modes (fiber splitting and kinking) become relevant. In this case, the stresses are rotated to the misalignment frame, where ψ and φ are determined to maximize the splitting and kinking criteria.

3.1.2. Concrete

The concrete behavior in FE model is defined by its elastic properties such as elastic modulus and Poisson's ratio, and the plastic properties using CDP model. CDP in ABAQUS [31] designed to simulate the complex behavior of concrete structures under various loading conditions. This model integrates the principles of plasticity and damage mechanics to capture the primary failure mechanisms in concrete, such as cracking under tension and crushing under compression. The CDP model is built on the foundation of elasto-plasticity theory, which traditionally decomposes total strain, ε, into elastic and plastic components:

$$\varepsilon = \varepsilon^{el} + \varepsilon^{pl} \tag{10}$$

However, concrete's nonlinearity arises from both damage and plasticity, necessitating a distinction between these effects in numerical simulations. The CDP model introduces a scalar damage variable d, ranging from 0 to 1, to represent the degradation of material stiffness. The stress-strain relationship in a damaged material is expressed as:

$$\sigma_{ij} = (1 - d)D_{ijkl}^{el}\left(\varepsilon_{ij} - \varepsilon_{ij}^{pl}\right) \tag{11}$$

Here, D_{ijkl}^{el} is the initial elasticity matrix, σ_{ij} is the stress tensor, and ε_{ij} and ε_{ij}^{pl} are the total and plastic strain tensors, respectively. For uniaxial loading, this relationship can be further simplified into separate equations for tension and compression:

$$\sigma_t = (1 - d_t)E_c(\varepsilon_t - \varepsilon_t^{pl}) \tag{12}$$

$$\sigma_c = (1 - d_c)E_c(\varepsilon_c - \varepsilon_c^{pl}) \tag{13}$$

where d_t and d_c are the tensile and compressive damage variables, respectively, and E_c is the initial elastic modulus, defined as $E_c = 4700\sqrt{f_c'}$ [22]. The yield surface in the CDP model defines the stress state beyond which plastic deformation initiates. The model adopts a yield criterion refined by Lubliner et al. [34] and Lee and Fenves [35], [36], expressed in terms of effective stresses:

$$F = \frac{1}{1-\alpha}(q - 3\alpha p + \beta\langle\sigma_{max}\rangle - \gamma\langle\sigma_{max}\rangle) - \sigma_c = 0 \tag{14}$$

where p is the hydrostatic pressure, and q is the Mises equivalent effective stress, σ_{max} is the maximum principal effective stress, and $\langle . \rangle$ denotes the Macauley bracket. The constants α, β, and γ are defined as:

$$\alpha = \frac{\frac{\sigma_{b0}}{\sigma_{c0}} - 1}{2\frac{\sigma_{b0}}{\sigma_{c0}} - 1} \tag{15}$$

$$\beta = \frac{\sigma_c}{\sigma_t}\frac{1-\alpha}{1+\alpha} \tag{16}$$

$$\gamma = \frac{3(1 - K_c)}{2K_c - 1} \tag{17}$$

Here, $\frac{\sigma_{b0}}{\sigma_{c0}}$ is the ratio of initial biaxial to uniaxial compressive yield stress, which was set to 1.16, and K_c has a default value of this parameter is 0.667 which was considered in the model (Figure 5).

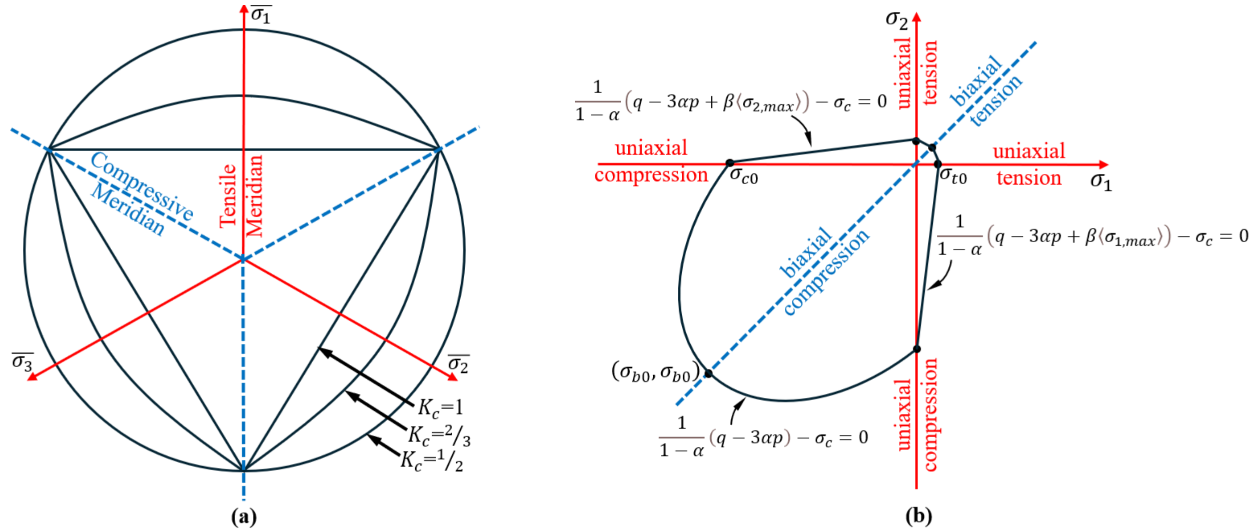

Figure 5 – CDP model: a) yield surface in the deviatoric plane, b) yield surface in plane stress

The hardening/softening behavior in the CDP model characterizes the pre- and post-peak responses of concrete. The hardening law describes the material behavior up to the peak stress, while the softening law governs the response beyond the peak. This behavior is typically defined in a tabular form relating yield stress to inelastic strain:

$$\varepsilon_c^{in} = \varepsilon_c - \frac{\sigma_c}{E_c} \tag{18}$$

$$\varepsilon_t^{in} = \varepsilon_t - \frac{\sigma_t}{E_c} \tag{19}$$

The software converts inelastic strain values to plastic strain values using the damage variables:

$$\varepsilon_c^{pl} = \varepsilon_c^{in} - \frac{d_c}{1-d_c}\frac{\sigma_c}{E_c} \tag{20}$$

$$\varepsilon_t^{pl} = \varepsilon_t^{in} - \frac{d_t}{1-d_t}\frac{\sigma_t}{E_c} \tag{21}$$

The flow rule in the CDP model determines the direction and magnitude of plastic deformation and is governed by a non-associated potential flow function with a Drucker-Prager type hyperbolic form:

$$G = \sqrt{(e\sigma_t tan\psi)^2 + q^2} - p(tan\psi) = 0 \quad (22)$$

Here, ψ is the dilation angle in the $p - q$ plane, and its initial value was set equal to 40°, σ_t is the uniaxial tensile stress, and e is the eccentricity parameter. This form ensures smooth and continuous potential flow, facilitating unique determination of the plastic strain rate:

$$\dot{\varepsilon}^{pl} = \frac{\partial G}{\partial \sigma} \quad (23)$$

For modeling the stress-strain relationship of concrete in compression, the constitutive model proposed by Popovics [37] was used:

$$f_c = f_c' \frac{\varepsilon_c}{\varepsilon_c'} \frac{n}{n - 1 + \left(\frac{\varepsilon_c}{\varepsilon_c'}\right)^n} \quad (24)$$

Wherein, f_c' is the concrete ultimate strength which was determined through standard cylinder tests on three samples per specimen, yielding a value of 42.0 ± 0.8 MPa, and n serves as the curve fitting number:

$$n = \frac{E_c}{\left(E_c - \frac{f_c'}{\varepsilon_c'}\right)} \quad (25)$$

ε_c' is the strain of concrete corresponding to its ultimate strength:

$$\varepsilon_c' = 1.7 \frac{f_c'}{E_c} \quad (26)$$

Damage was assumed to occur solely within the softening range, with its parameters applied to both tension and compression [38]. The tensile behavior of concrete is modeled using a descending bi-linear trend, starting from the maximum tensile strength f_t and decreasing to $0.2f_t$ at a crack width displacement of G_f/f_t, where G_f is the fracture energy of the concrete, defined as the area under the tensile stress-crack displacement curve. This approach helps mitigate the sensitivity of the results to mesh size [39]. The fracture energy G_f for normal-weight concrete can be calculated using [40]:

$$G_f = G_{f0}\left(\frac{f_c' + 8}{f_{cmo}}\right)^{0.7} \tag{27}$$

wherein, the parameters f_c' and f_{cmo} are both expressed in MPa, with f_{cmo} set to 10 MPa. The base fracture energy G_{f0}, which is dependent on the maximum aggregate size, was determined to be 0.03 for the 12 mm (½") aggregate size used in specimen preparation [40]. Additionally, in the CDP model, the viscosity parameter μ, was assigned a value of 0.00001 s to enhance the convergence of the analysis. The initial values for the CDP model parameters were selected based on previous studies on reinforced concrete models [40], [41], [42], [43] and then refined through calibration using the experimental results of this study. Table 3 summarizes the final mechanical properties used in the CPD model.

Table 3 – Summary of calibrated concrete mechanical properties used in the FE models

f'_c (MPa)	ε_c' (μm/m)	E_c (MPa)	Poisson's ratio (ν)	G_f (N/mm)	ψ	$\frac{\sigma_{b0}}{\sigma_{c0}}$	K_c	ρ (tonne/mm^3)
42	0.0023	30460	0.2	0.093	35°	1.16	0.667	2.35×10^{-9}

The values of $\frac{\sigma_{b0}}{\sigma_{c0}}$ and K_c were set to 1.16 and 0.667, respectively, as these values were consistently used in prior studies [40], [41], [42], [43]. Value of ψ varied in previous studies, ranging from 31° [41] to 40° [40], with 35° being calibrated in [42]. In this study, a value of 35° was adopted after calibration to balance convergence stability and accuracy. μ plays a critical role in improving numerical stability in the CDP model. While previous studies used values between 0 and 0.0003 [40], [41], [42], a calibrated value of 0.0001 was used in this study to ensure a balance between damping effects and computational efficiency. G_f was computed based on concrete strength and mesh sensitivity considerations, following approaches used in previous studies [43]. The characteristic length was defined as the element volume divided by the largest face area, ensuring a consistent strain distribution across different mesh sizes.

3.2. Model Geometry and Discretization

The FE models resembled experimental specimens, with few simplifications applied. As illustrated in Figure 6, the models incorporated concrete, reinforcing bars, and ties, all represented using 8-node linear brick 3D solid elements with reduced integration and second-order accuracy. This approach enables a more accurate representation of stress and strain distributions within each element by utilizing higher-order interpolation functions. Also, enhanced hourglass control was activated. Hourglass modes are non-physical, zero-energy deformation patterns that can arise in reduced integration elements, potentially leading to inaccuracies and numerical instability. The enhanced hourglass control implemented in the C3D8R elements effectively mitigates these issues, ensuring that the elements deform in a physically realistic manner under loading conditions.

The geometric configuration of the models was designed to replicate the dimensions and shapes of the experimental specimens accurately. The concrete core was modeled as solid volumes, with reinforcing bars exposed on four edges and ties holding the longitudinal bars. Mesh generation was carried out using a sweep technique. This method involves generating a structured mesh by sweeping a 2D mesh along a specified path, which ensures a uniform and consistent element distribution. The sweep meshing approach was used to optimize the mesh density, balancing computational efficiency and accuracy. Finer meshes were applied in regions with expected high stress gradients, such as around the reinforcing bars and at material interfaces.

Mesh sensitivity in the CDP model is often associated with the localization of strains, where the results can become overly dependent on the mesh size, especially when dealing with strain-softening behavior. Regularization methods like non-local averaging or the use of damage regularization techniques are typically employed to address this issue, ensuring that the results are less sensitive to mesh refinement. The latter was considered in the property definition for concrete, while for the nonlocal averaging, instead of calculating the strain or damage at a single integration point based solely on local values, the variables are averaged over a finite region surrounding the point. This region is often defined by a characteristic length, which controls the extent of the averaging. The characteristic length, l_c, is defined as the element volume divided by the area of its largest face. This definition helps to capture the dominant length scale of the element, especially in cases where the element is not perfectly cubic. In regions where local mesh refinement is applied, such as around sharp edges or regions with high stress gradients, the aspect ratio of the elements tends to decrease, leading to a characteristic length that more closely approximates the element's physical size.

3.3. Boundary Conditions and Analysis Method

FE models employed displacement/rotation boundary conditions to restrict specific degrees of freedom at the boundaries, ensuring it closely resembled the experimental setup. To simulate fixed support conditions, all degrees of freedom were constrained at the bottom, reflecting the experimental scenario where no slip or rotation occurred. This model represents a segment of a longer column, assuming failure occurs within this portion, such as at mid-height. Similar constraints were applied to the top surface, with an additional displacement in the third degree of freedom (z direction) to simulate compressive loading. These constraints ensured the structure was properly supported, directing the applied loads through the intended paths and accurately replicating the experimental conditions.

The simulation was carried out using a static analysis approach within ABAQUS, where non-linear geometric effects were considered. The step settings were defined as a static analysis step with an initial time increment of 1×10^{-6}, a maximum time increment of 0.01, and a minimum increment size of 1×10^{-10}. These settings provided a balance between computational efficiency and accuracy, allowing the model to capture the detailed response under applied loads, particularly in the sensitive time steps in the beginning of the simulation. Field outputs such as reaction forces, displacements, and element-based outputs, including stress, strain, and damage variables, were requested at specified intervals to monitor the performance and failure mechanisms of the columns.

A surface-to-surface contact formulation was used for the contact between concrete and the longitudinal bars. Cohesive contact properties were applied, following the behavioral model introduced by Alves et al. [44]. For the interaction between the longitudinal bars and the ties, a surface-to-surface contact with hard contact properties was utilized. Additionally, the ties' interaction with the concrete was also modeled as a surface-to-surface hard contact but with a distinct friction coefficient to account for the differing interaction characteristics.

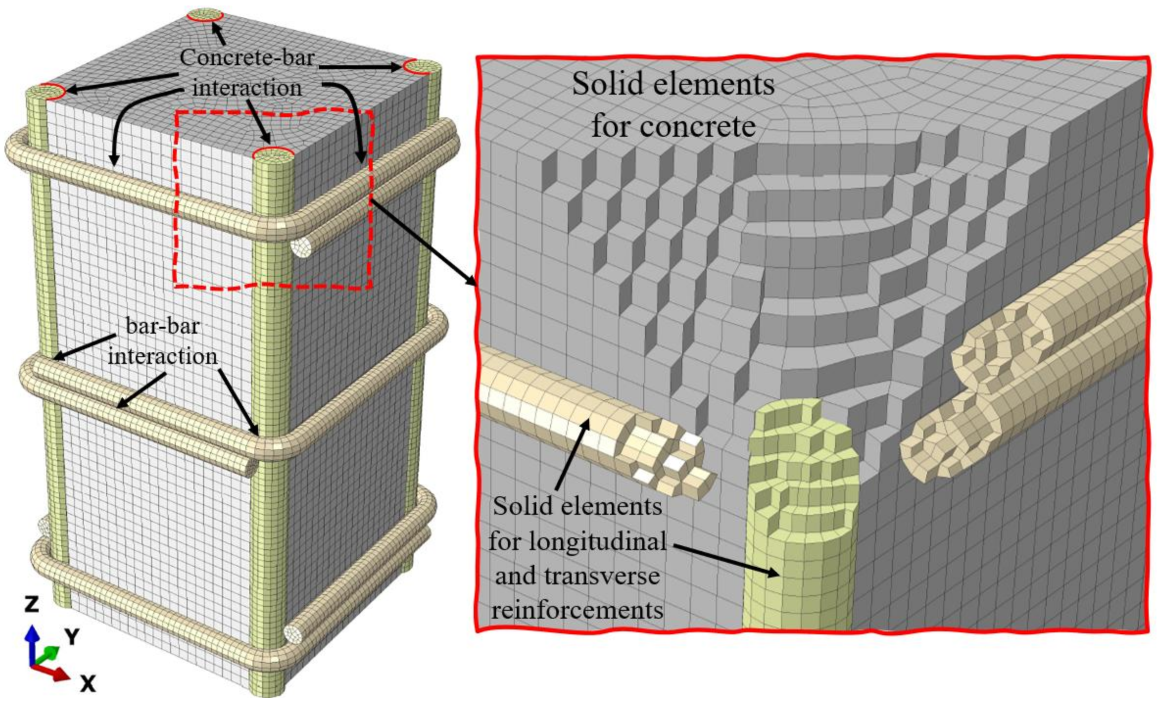

Figure 6 – FE model mesh geometry

4. EXPERIMENTS AND FE MODELS RESULTS

This section presents the analysis and interpretation of the results. Figure 7 compares the failure patterns of the test specimens with those predicted by the finite element (FE) models at the final loading stage. Figure 7a illustrates the failure pattern of the plain concrete specimen (PC) when the applied load had decreased to 70% of its peak value. The top image shows the test specimen after failure, displaying visible cracks and surface spalling, while the other two present concrete damage contours from the FE models, comparing cases with and without (bottom image) surface defects. In the test specimen, the failure is characterized by prominent cracking in the central region of the column, indicative of the high stress concentration typically encountered in this area during axial compression. The middle section experiences the greatest compressive stress, leading to material crushing and crack propagation. The observed damage aligns with the expected failure mode for concrete under significant compressive loads. The finite element model with negligible initial defects on the surface reveals a non-uniform distribution of damage.

The damage contours highlight regions of high damage (red zones) concentrated in the central area of the column, similar to the test specimen's failure pattern. The presence of minor surface defects seems to create a more realistic representation, closely resembling the test specimen. In contrast, the FE model without surface defects exhibits a more symmetrical and uniform damage distribution. While the central region still shows the highest concentration of damage.

Figure 7b presents a comparison between the results of R-S100-T20-1 test specimen (top) and the corresponding FE model results (middle and bottom) displaying damage contours for the concrete (middle) and the GFRP bars (bottom). In the test specimen, significant concrete crushing is evident, particularly in the central region of the column. Failure is characterized by extensive cracking and spalling of the concrete, along with visible opening of the ties and local buckling of the GFRP bars. The deformation and opening of the ties indicate that the lateral confinement from the GFRP bars was surpassed by internal pressure from the expanding concrete, resulting in failure occurring well after the peak load was observed. The FE model of the concrete (middle image) illustrates the compressive damage variable, showing a similar pattern of failure. The highest concentration of damage (red regions) occurs in the central portion of the column. On the bottom, the FE model provides damage contours for the GFRP bars, using LARCFKCRT. The results show significant damage in areas where the GFRP bars are most likely to buckle and fail, particularly around the ties. The model predicts localized buckling of the GFRP bars, corresponding to the observed deformation and failure of the ties in the test specimens.

Figure 7c shows the failure pattern in R-S100-T20-2 (top) alongside the corresponding FE model results (middle and bottom). In the test specimen, large cracks and concrete spalling were observed following the opening of the ties. The visible deformation and the separation between the GFRP ties suggest that the ties have been pushed outward as the concrete expanded and cracked at post peak, leading to buckling of the reinforcement. The middle image, which displays DMAGEC, shows a damage pattern that closely mirrors the physical test results. On the bottom, the FE model displays LARCFKCRT for the bars. This contour highlights areas where the GFRP bars are most susceptible to damage, particularly at the locations where the ties are situated. The model indicates significant damage in these regions after tie opening, which correlates with the observed buckling and failure of the ties in the test specimen. The outward buckling and opening of the ties seen in the physical test are effectively captured by the FE model.

Figure 7d compares the failure behavior of R-S100-T28-1 with a longer tie overlap length (top) to the corresponding FE model results (middle and bottom). The test specimen shows cracking and concrete spalling, particularly in the central region. The longer overlap length of the ties played a critical role in providing integrity in the GFRP reinforcement. The failure pattern in the longitudinal bars is similar to the previous specimens however, the failure occurred at larger axial, and correspondingly lateral deformation. The FE model in the middle image, displaying DMAGEC, show the concentration of damage in the central region, where the compressive stresses are greatest, which corresponds to the actual damage observed in the physical specimen. The bottom image from the FE model shows LARCFKCRT for the longitudinal bars. The longer overlap length of the ties is reflected in the FE results, where the regions of highest damage in longitudinal bars shifted from the center providing higher resistance to buckling.

Figure 7e compares the test results of R-S200-T28-1 with 200 mm tie spacing (top) to the corresponding FE model results (middle and bottom). The 200 mm spacing between ties (about 12d_b), which is double the spacing of the previous specimens, results in less effective confinement, as evidenced by the larger and more pronounced cracks. The wider spacing allows for greater lateral expansion of the concrete. The visible buckling of the bars suggests that the increased tie spacing has reduced the overall structural integrity, making the column less deformable under compressive loads. The middle image, which displays DAMAGEC for the concrete, shows a damage pattern in which the highest concentration of damage is again located in the central region of the column, where the concrete experiences the greatest compressive stresses. The bottom image from the FE model shows LARCFKCRT for the GFRP bars. The wider tie spacing is reflected in the FE results, where the regions of highest damage are concentrated at the locations of the ties. The model predicts significant fiber kinking in these areas, consistent with the observed deformation and failure of the longitudinal bars in the test specimen. This observation is in-line with the brittle failure reported by Abbas et al. [45] for large-scale columns with similar tie spacing.

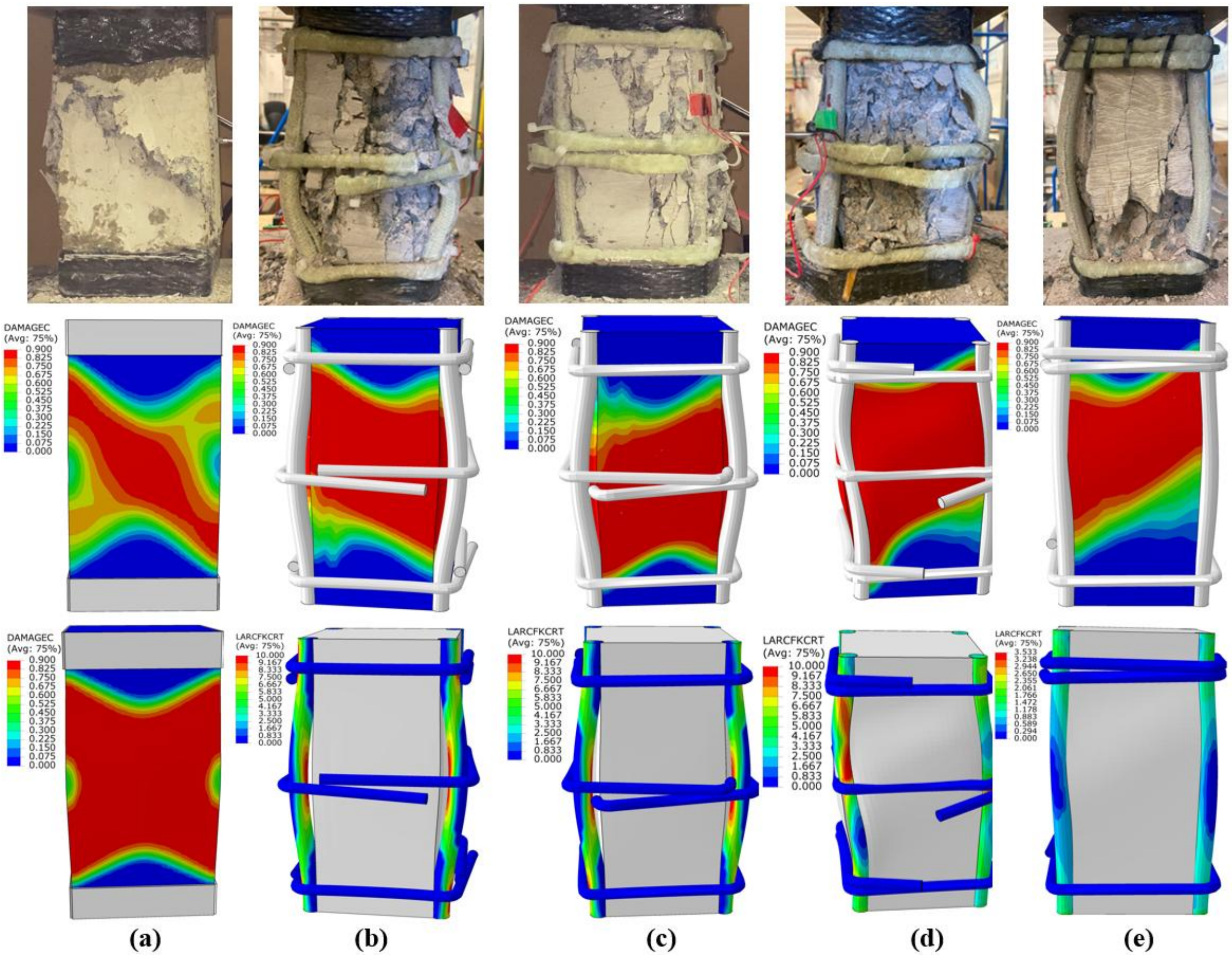

Figure 7 – Comparing the failure patterns in the test specimens and FE models: a) PC, b) R-S100-T20-1, c) R-S100-T20-2, d) R-S100-T28-1, and e) R-S200-T28-1

Figure 8 shows the hoop stress pattern in the concrete core at an equal loading. This shows a more uniform distribution of hoop stress in the specimens with less tie spacing. The pattern of stress distribution follows the pattern of confined core which is besieged in the post-peak.

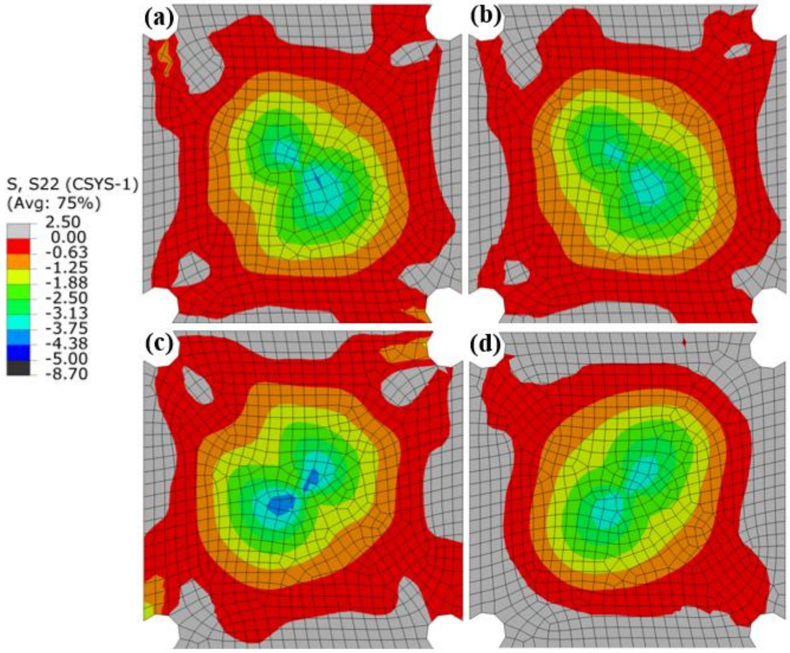

Figure 8 – Comparison of the compressive hoop stress pattern in cylindrical coordinate system in the FE models: a) R-S100-T20-1, b) R-S100-T20-2, c) R-S100-T28-1, and d) R-S200-T28-1

Figure 9 reveals significant differences in performance related to tie spacing, highlighting the stress-strain behavior of GFRP-RC columns for tests and FE models with various tie configurations, overlap lengths, and arrangements compared to specimen PC, which reflects the expected behavior for unreinforced concrete following the behavior in Eq. (24).

Specimens R-S100-T20-1 (Figure 9a) and R-S100-T20-2 (Figure 9b), with identical tie spacing of 100 mm (around $6d_b$) and overlap lengths ($20d_t$) but different tie configuration, demonstrate similar behavior, characterized by a sudden drop in stress following the peak, indicative of brittle failure in concrete and then gaining strength after experiencing large strains. The key difference between these two specimens is that R-S100-T20-1 exhibited higher strength at both the peak load and post-peak stages, suggesting the greater effectiveness of closed GFRP ties cut from continuous square ties compared to C-shaped ties. Tobbi et al. [10] reported a similar observation; however, it is important to note that the method of securing C-shaped ties together also affects post-peak strength.

Specimen R-S100-T28-1 (Figure 9c), which has a larger tie overlap length of 28d_t, displays an improved post-peak performance, maintaining its load-carrying capacity longer and reaching higher strengths at the second peak. This suggests that the increased overlap length enhances confinement and delays the onset of longitudinal bar buckling. However, the effect of tie configuration on the first peak load is negligible. Specimen R-S200-T28-1 (Figure 9d), featuring a larger tie spacing of 200 mm (around 12d_b) and ties only at the top and bottom, shows less stable post-peak behavior with an earlier drop in stress compared to the other specimens due to lack of lateral support for bars and insufficient confinement for the core.

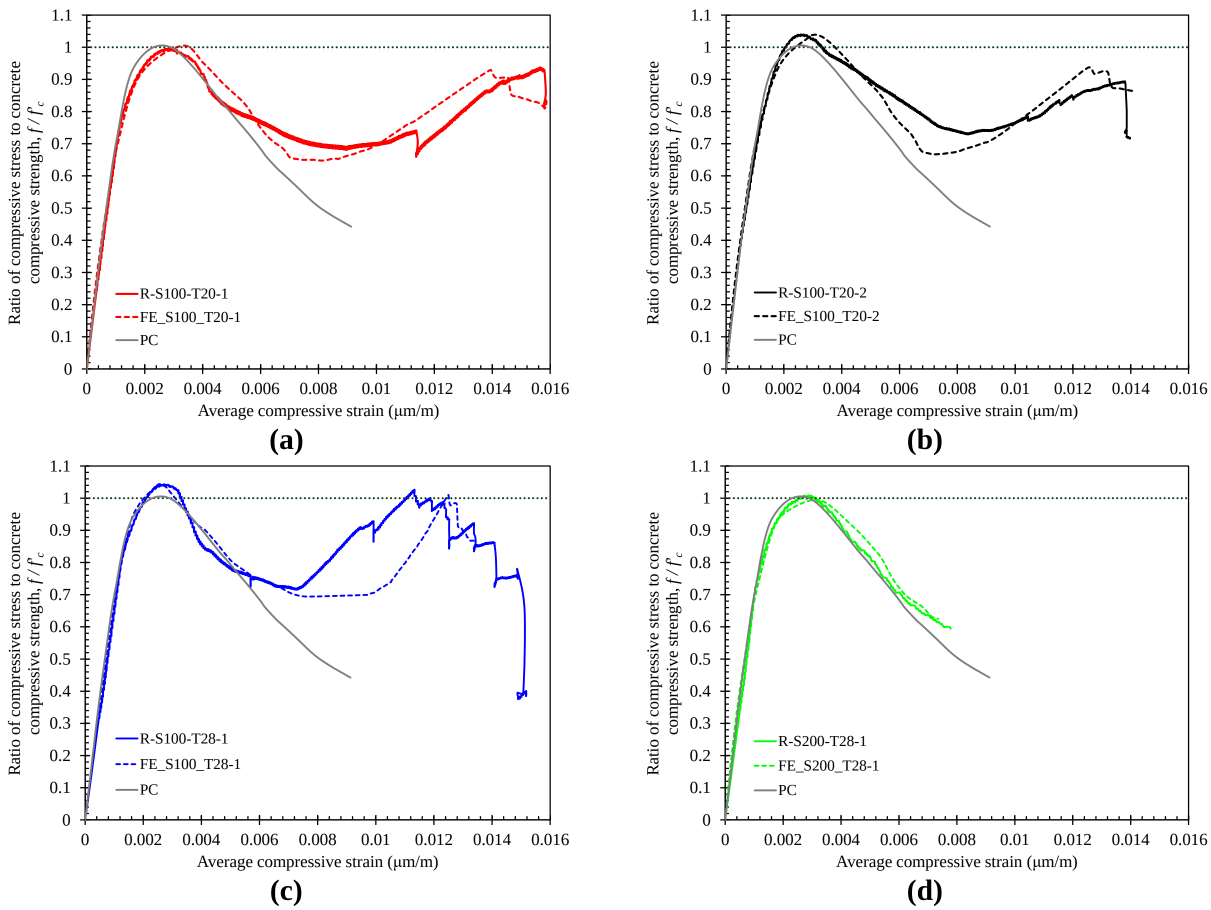

Figure 9 – Ratio of compressive axial stress to concrete strength as a function of axial strain for the specimens: a) R-S100-T20-1, b) R-S100-T20-2, c) R-S100-T28-1, and d) R-S200-T28-1

Overall, while the spacing of ties is a significant factor in the buckling pattern of longitudinal bars, other parameters, such as the stiffness of the ties, also play a crucial role. Stiffer ties provide greater lateral support, which is essential for maintaining the stability of the bars under load. Higher integrity of the bars is achieved through increased overlap length, as observed in both experimental tests and confirmed by FE models. Specifically, a $28d_t$ overlap results in better post-peak behavior, characterized by a higher second peak load and increased energy absorption.

The stiffness of the ties is a crucial design factor, particularly for controlling post-peak behavior and preventing premature failure. An important aspect of GFRP ties is the inclusion of hooked ends, with test results showing that having two hooks on both sides of the tie is necessary to maintain structural integrity. Given the 90^{o} hook angles in GFRP bars, a minimum hook length of $6d_t$ is required which is suggested to be increased to $12d_t$ as the development length required for GFRP bars in tension [22]. Furthermore, the use of zip ties to secure the tie bars significantly influences the overall stiffness and performance of the ties. This study observed that using common heavy duty zip ties with a $3d_t$ interval enhances the ties' integrity and functionality well beyond the first peak load.

5. DEFORMABILITY

Deformability allows concrete columns to deform significantly without sudden failure, ensuring energy absorption and structural safety. Confinement through transverse reinforcement, such as ties or spirals, enhances both axial load capacity and ductility by preserving the concrete core under deformation, especially during seismic events. However, the lower ductility of GFRP bars compared to steel makes proper confinement and design even more critical for maintaining energy dissipation and load-carrying capacity, as required by modern seismic standards.

For the use of FRP bars and ties in concrete columns under concentric loading, studies by Tobbi et al. [8], Hadi and Youssef [46], Mohamed et al. [15], De Luca et al. [3], and Abed et al. [47] were considered since they tested columns with ties or hoops and provided stress-strain diagram or axial load- displacement of the column in their test results which are needed to measure the required parameters in calculating the deformability index. Table 4 provides a summary of the parameters from the studies considered.

Table 4 – Summary of parameters for the tested specimens in the literature, used for deformability analysis

Study	Specimen ID	Cross-section shape	Dimensions (mm)	f_c (MPa)	Reinforcement type	Longitudinal reinforcement	Transverse reinforcement	s (mm)	P_{max} (kN)	$P_{max,2}$ (kN)	Diagram category
Tobbi et al. [8]	C-G-1-120	Square	350×350	32.6	GFRP	Eight No. 6	No.13	120	3920	—	1
	C-G-1A-120	Square	350×350	32.6	GFRP	Eight No. 6	No.13	120	4005	—	1
	C-G-2-120	Square	350×350	32.6	GFRP	Eight No. 6	No.13	120	4005	—	1
	C-G-3-120	Square	350×350	32.6	GFRP	Twelve No. 5	No.13	120	3941	—	2
	C-G-3-80	Square	350×350	32.6	GFRP	Twelve No. 5	No.13	80	3909	4069	3
Hadi and Youssef [46]	RF-0	Square	210×210	33.0	GFRP	Four No. 4	No.3	50	1285	—	2
Mohamed et al. [15]	G3H200	Circular	D=300	42.9	GFRP	Eight No. 5	No.3	80	2840	—	1
	G3H400	Circular	D=300	42.9	GFRP	Eight No. 5	No.3	80	2871	—	1
	G3H600	Circular	D=300	42.9	GFRP	Eight No. 5	No.3	80	2935	—	1
	C3H200	Circular	D=300	42.9	CFRP	Ten No. 4	No.3	80	2869	—	1
	C3H400	Circular	D=300	42.9	CFRP	Ten No. 4	No.3	80	2960	—	1
	C3H600	Circular	D=300	42.9	CFRP	Ten No. 4	No.3	80	3008	—	1
De Luca et al. [3]	A-3	Square	610×610	34.5	GFRP	Eight No. 8	No.4	76	5236	—	1
	B-3	Square	610×610	34.5	GFRP	Eight No. 8	No.4	76	4763	—	1
Abed et al. [47]	G20-B-180	Square	180×180	38.3	GFRP	Four No. 6	No.3	180	986	—	1
	G20-B-120	Square	180×180	38.3	GFRP	Four No. 6	No.3	120	1005	—	2
	G20-B-60	Square	180×180	38.3	GFRP	Four No. 6	No.3	60	1030	954	3
	B20-B-180	Square	180×180	38.3	BFRP	Four No. 6	No.3	180	955	—	1
	B20-B-120	Square	180×180	38.3	BFRP	Four No. 6	No.3	120	1044	—	2
	B20-B-60	Square	180×180	38.3	BFRP	Four No. 6	No.3	60	1033	1041	3

A general look at these studies showed that the shape of the diagram matches one of the three categories in Figure 10. Either the load goes up until peak load and drops suddenly which is mainly due to the longitudinal buckling and crushing after the opening or rupture of ties. The second category is for the state that the column shows more ductility and withstands a load which is within 85% of the peak load [47], [48] and then failure after a deformation in a sustained load. This type of failure occurs in columns with more intricate tie configurations and reduced tie spacing, which offer significant passive confinement for the core concrete following the spalling of the concrete cover. The failure manifests as longitudinal crushing. The third category is achieved when the column is heavily reinforced longitudinally and in transverse direction and the confinement effect is fully developed in such a way that a second peak load is observed after relatively long deformation in a sustained load. The failure is in the form of core concrete crushing, crushing of the longitudinal bars and tie rupture.

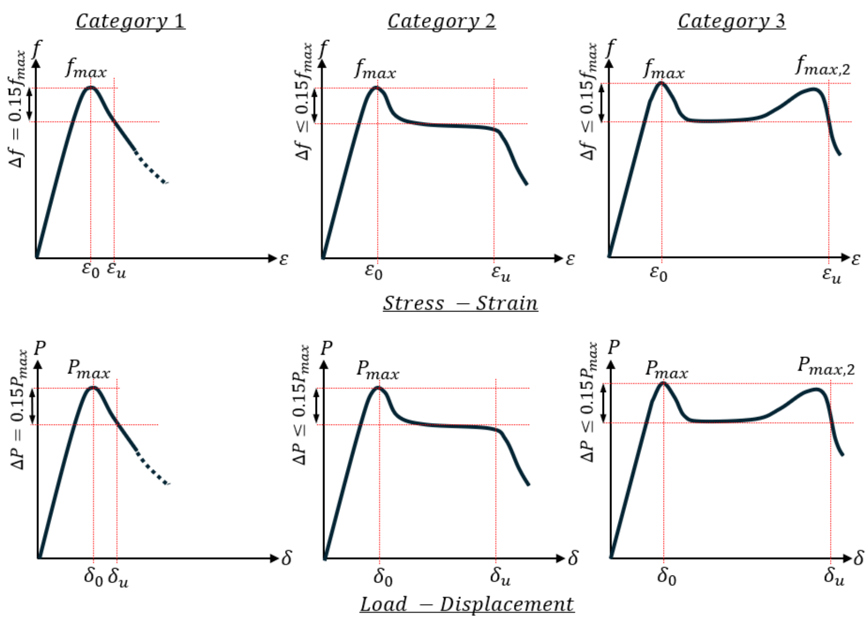

Figure 10 – Three general post-peak behaviors that were observed in GFRP-reinforced concrete columns

Observations from the tests (Figure 7) and the corresponding stress-strain behavior (Figure 9) indicate that a tie spacing of $12d_b$ (R-S200-T28-1) results in minimal deformability, similar to Category 1 in Figure 10. In contrast, a tie spacing of $6d_b$ with sufficient hook length (R-S100-T28-1) leads to significantly higher deformability, aligning with Category 3.

Based on the literature, the most common tie configurations are shown in Figure 11, with Config. 1 being the most widely used. This configuration also represents circular hoops, as studied by Mohamed et al. [15]. Various scenarios related to tie construction were considered in this study, and the effect of overlapping was examined in the final section. However, the focus here is on the geometry of the ties in plan view. The literature suggests a rational correlation between the complexity of the tie configuration and the level of confinement provided. To investigate this relationship, the transverse reinforcement ratio $\rho_t(\%)$ (not volumetric) was determined for the test specimens from the referenced studies using:

$$\rho_t(\%) = \frac{100nA_t}{bs} \tag{28}$$

Wherein, n is the number of tie cross-sections, A_t is the cross-sectional area of tie, b is the larger dimension of the column cross section in rectangular columns and diameter in circular columns, and s is the center-to-center tie spacing.

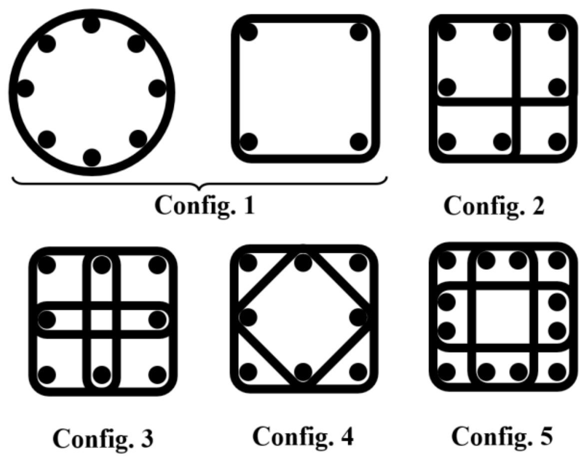

Figure 11 – Common tie configurations used in GFRP-reinforced concrete columns

Based on the provided load-displacement or stress-strain diagrams, δ_0 and δ_u, or ε_0 and ε_u, were extracted from the diagrams following the methodology outlined in Figure 10. Having δ_0 and δ_u, or ε_0 and ε_u, the axial deformability of the column was calculated using Eq. (29). This equation represents the ratio of axial displacement/strain after the peak load to the total axial displacement/strain recorded up to failure, which was assumed to occur at 85% of the peak load:

$$I_{AD} = \frac{\varepsilon_u - \varepsilon_0}{\varepsilon_u} \; or \; \frac{\delta_u - \delta_0}{\delta_u} \tag{29}$$

In Eq. (29), I_{AD} is always less than 1 and represents the proportion of the total deformation that occurs beyond the peak load. Figure 12 illustrates the relationship between I_{AD} and $\rho_t(\%)$. As shown, there is a significant relationship between the transverse reinforcement ratio and the axial deformability of the column, which can be represented by a linear trend. Based on this figure, the deformability index can be calculated as a function of the transverse reinforcement ratio using:

$$I_{AD} = 0.51\rho_t(\%) - 0.20 \tag{30}$$

This relationship provides a preliminary estimate of the level of deformability achievable in a column under concentric loading, assuming longitudinal bars are placed at every corner or junction of the ties. This estimation relies on the transverse reinforcement ratio, with the shaded areas in the figure roughly corresponding to the graph categories defined in Figure 10.

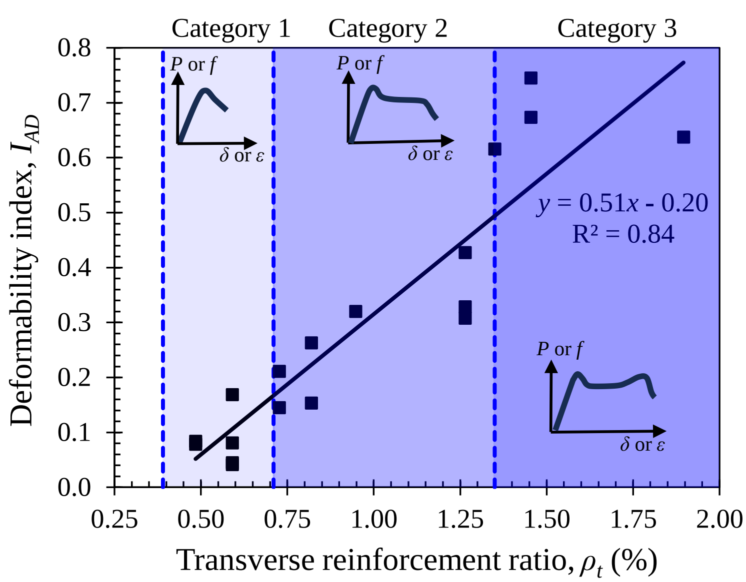

Figure 12 – Relationship between deformability index, I_{AD}, and transverse reinforcement ratio, $\rho_t(\%)$ for test specimens

6. DISCUSSION

6.1. Effective Tie Spacing

The effectiveness of tie spacing in GFRP-reinforced concrete columns significantly depends on the ties' stiffness, continouity and configuration. Jawaheri Zadeh and Nanni [1] proposed a simplified model that assumes pin-pin support between ties while disregarding the effect of concrete cover on providing any lateral support. They calculated a maximum spacing of approximately $14d_b$ to achieve the desired strain levels and recommended reducing it to $12d_b$ for safety, in line with De Luca et al. [3]. However, this model does not account for deformation in the ties due to the lateral deformation of the concrete. This deformation manifests as tensile strain in seamless ties and as a combination of tensile strain and overlap slip in overlapped ties, such as C-shaped ties or those with insufficient hook lengths. Even minor deformation can reduce the effectiveness of lateral support, making the longitudinal bars more prone to buckling.

Abbas et al. [45] argued that a tie spacing of $12d_b$ leads to brittle failure in GFRP-reinforced columns, while reduced spacing of $6d_b$ to $8d_b$ results in a more ductile response, with $8d_b$ being optimal for balancing peak load and ductility. Similarly, Tobbi et al. [8] observed improved ductility and a delayed strength drop at a tie spacing of around $7.5d_b$, with further reductions to $5d_b$ leading to a second peak at large strains.

This study's observations align with these findings, showing that ties with a $28dt$ overlap can maintain sufficient support with a $12d_b$ spacing, although $6d_b$ spacing leads to the emergence of a second peak and ensures ductility [8]. For less discontinuous ties, such as C-shaped ties or those with shorter hook lengths (around $20d_t$), the assumption of pin-pin support becomes less applicable. The stretch of these softer ties under concrete lateral pressure reduces their ability to provide adequate lateral support, effectively doubling the unsupported length between ties.

Consequently, for discontinuous configurations, a maximum tie spacing of $6d_b$ instead of $12d_b$ may be considered to provide adequate support and avoid premature failure. Furthermore, the spacing and quality of fasteners, such as zip ties, are essential to the overall performance.

This study is limited to specific fastener types and their intervals for different column sizes. Further research is recommended to investigate the effects of tie elastic modulus, strength, and spacing in the overlapped regions to provide additional data for future incorporation into design codes.

6.2. Deformability

An example was analyzed for two different configurations of longitudinal and transverse reinforcement. In the first configuration, #5 straight bars served as longitudinal reinforcement, while #3 bars were used for ties. In the second configuration, #8 bars were employed for longitudinal reinforcement, with #4 bars for ties. The nominal cross-sectional areas of the #3, #4, #5, and #8 bars are 71.26, 126.68, 199, and 510 mm², respectively. For each case, three column cross-sectional dimensions (200, 300, and 400 mm) were considered. Three different tie spacings (s=$6d_b$, $8d_b$, and $12d_b$) were evaluated for different tie configurations: n=2 and n=3 correspond to Config. 1 and 2 in Figure 11, while n=4 corresponds to Configurations 3, 4, and 5. The results are shown in Figure 13. As indicated, the ductility index, I_{AD}, thresholds are based on the ρ_t(%) ranges in Figure 12. The transverse reinforcement ratios at the boundaries of each category were identified based on the stress-strain or load-deformation curves from reference tests, and the corresponding I_{AD} values were calculated using Eq. (30). For example, I_{AD}=0 corresponds to ρ_t=0.39%, I_{AD}=0.16 corresponds to ρ_t=0.71%, and I_{AD}=0.49 corresponds to ρ_t=1.35%.

The results show that for s=$12d_b$, the likelihood of achieving moderate deformability is significantly lower than for s=$6d_b$ or s=$8d_b$. At s=$6d_b$, the column generally exhibits deformability, except when using large sections (400×400 mm) with #5 longitudinal bars and #3 tie bars in Config. 1 (Figure 11).

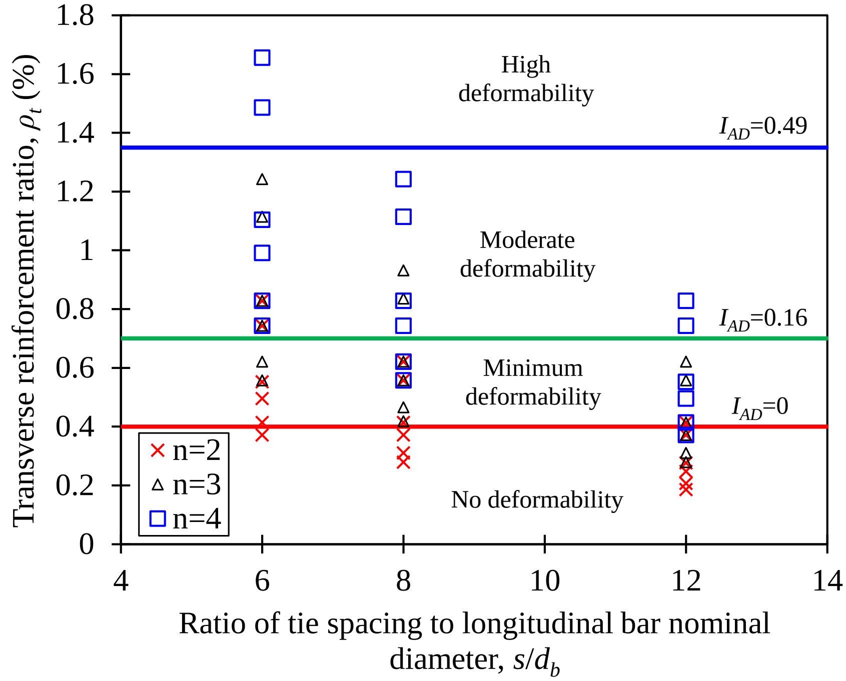

Figure 13 – Example illustration of the deformability ranges for columns with various s/d_b and $\rho_t(\%)$ for different number of tie cross sections, *n*

Hadi et al. [21] defined deformability as the ratio of the area under the axial load–deformation curve up to ultimate deformation to that up to the end of the linear elastic stage, emphasizing overall energy absorption. In contrast, our method calculates deformability as the difference between ultimate deformation (at 85% post-peak load drop) and peak deformation, divided by ultimate deformation, focusing on post-peak deformation capacity. While Hadi et al.'s approach assesses overall ductility, our method directly quantifies post-peak stability in GFRP-RC columns.

Two FEM approaches for GFRP-RC columns are compared and discussed here in terms of various parameters such as ease of modeling, computation costs, and accuracy of the predictions. In the first approach (Approach A), using the FEM framework that was developed in this study, models of the test specimens by Tobbi et al. [8] were prepared and analyzed. The models were prepared for a quarter of the specimens and YZ and XZ planes are symmetry planes. Figure 14 illustrates the simplified bar cages prepared for five different scenarios. The ties spacing, S, of 80 and 120 mm from C-G-3 specimens [8] were used for checking the model, and the rest, with S=100, 95, 130 mm was prepared to cover ρ_t= 0.76, 1.6, 1.17 %, respectively.

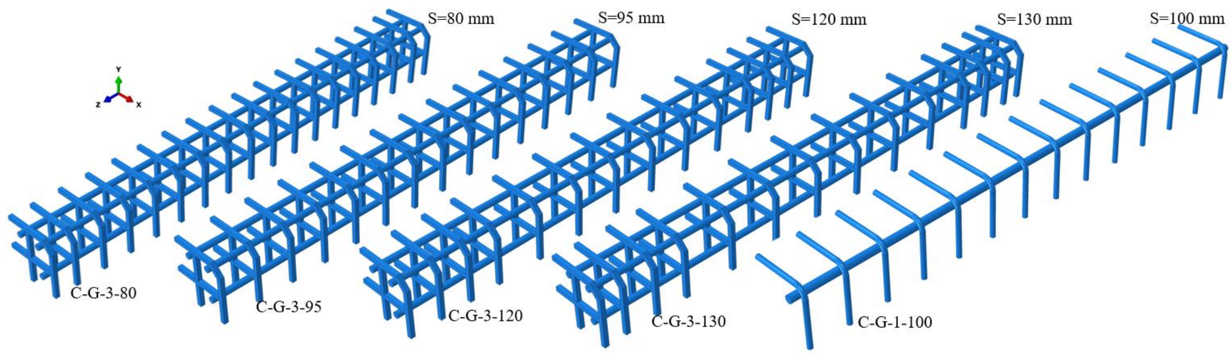

Figure 14 – Reinforcement geometries in the FE models (Approach A)

Figure 15 illustrates the damage contours for concrete and reinforcement at the failure point for specimen C-G-3-130, serving as a representative example. DAMAGEC contours indicate that failure occurred primarily at mid-height, manifesting as inclined cracks. Initial damage to the concrete cover occurred after the peak load, consistent with observations from experimental studies in literature. Longitudinal bar damage (LARCFKCRT) also initiated after the peak load, with failure occurring after cracks were observed in the transverse reinforcement. LARCMCCRT for the transverse reinforcements display higher maximum values compared to the damage in the longitudinal bars, indicating the extent and sequence of damage propagation in the specimen.

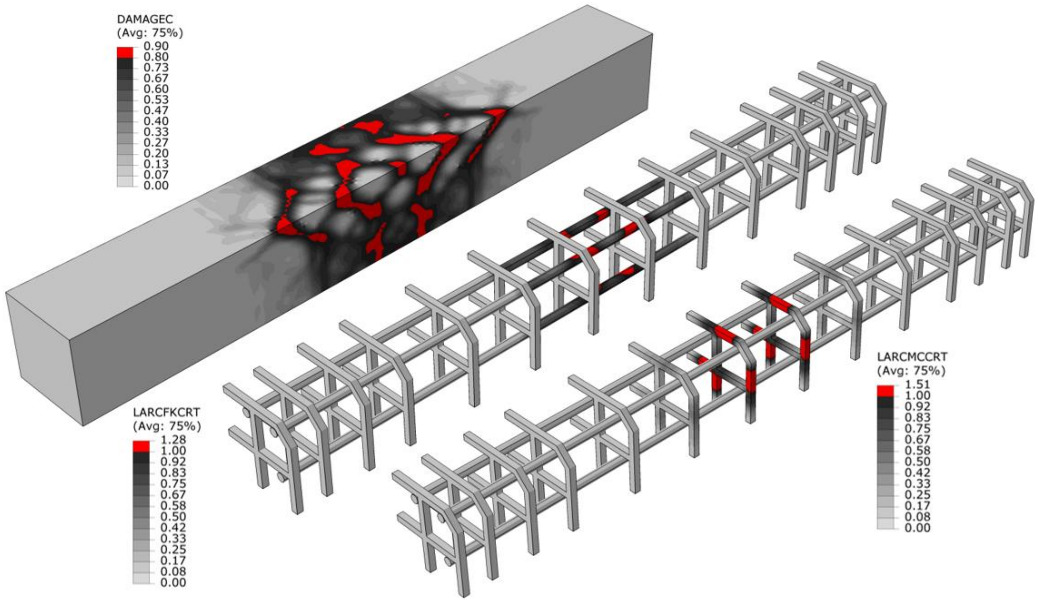

Figure 15 – Contours of DAMAGEC, LARCFKCRT for longitudinal bar, and LARCMCCRT for transverse reinforcement in C-G-3-130

In the second approach (Approach B), a widely adopted finite element modeling technique for reinforced concrete members was employed, with further refinements to enhance accuracy. This approach treats concrete as a continuous solid part using three-dimensional elements (e.g., C3D8R) with enhanced hourglass control and considering second-order accuracy in the analysis, while the reinforcement is represented by one-dimensional beam elements (e.g., B32) embedded within the concrete matrix.

The embedded element technique in Abaqus ensures kinematic compatibility by constraining the translational degrees of freedom of the reinforcement nodes to the interpolated displacements of the surrounding concrete elements. This method allows for efficient modeling of reinforced concrete structures while maintaining a reasonable computational cost.

The reinforcement cages, modeled using beam elements, are depicted in Figure 16 in their rendered form. Figure 17 presents the stress distribution in the reinforcement and the damage contours in the concrete at the point of failure.

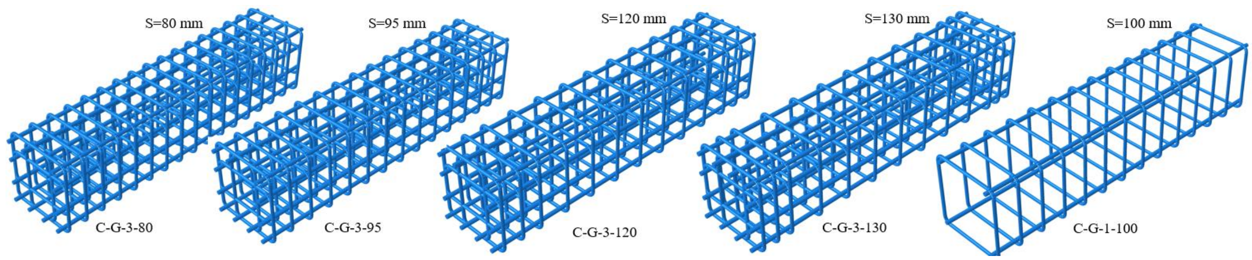

Figure 16 – Rendered reinforcement geometries in the FE models (Approach B)

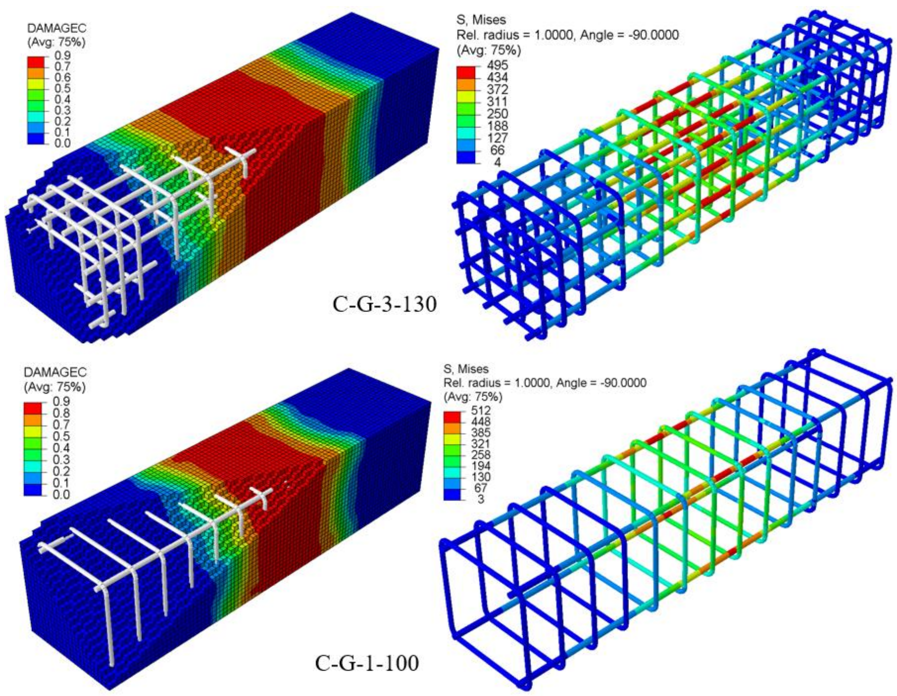

Figure 17 – Stress and damage contours in the FE models at failure point (Approach B)

Figure 18 compares FEM results from both approaches with experimental tests for the axial stress-strain behavior of columns C-G-3-80 and C-G-3-120. According to Figure 18a for Approach A, the FEM accurately captures the initial linear elastic region and peak load, closely aligning with the test data. In the post-peak region, it successfully predicts the failure point; however, the post-peak behavior is underpredicted due to modeling simplifications. Despite this, the FEM effectively captures the relative difference in confinement effects between C-G-3-80 and C-G-3-120, mirroring the trends observed in the tests. This indicates that while the FEM underestimates post-peak stress, it remains useful for comparative analysis of tie spacing and confinement effects.

Considering the computational cost of modeling the detailed 3D geometry in Approach A, Approach B was also used, and the results were compared with the tests in Figure 18b. As shown, the FEM overestimates the initial slope but demonstrates good agreement in predicting the peak load. In the post-peak region, it captures the load drop with reasonable accuracy; however, the failure point is not precisely predicted.

Regarding FEM performance, Approach A is suitable for predicting the initial stiffness, peak load, and failure onset, while Approach B is more effective in capturing the post-peak load drop. Three additional tie configurations—C-G-3-95, C-G-3-130, and C-G-1-100—were modeled, with their axial stress-strain behaviors presented in Figure 19 for both approaches. The model for C-G-3-95, which has closer tie spacing than C-G-3-130, demonstrates higher post-peak axial stress, indicating better confinement and enhanced load-carrying capacity. Conversely, C-G-3-130, with wider tie spacing, exhibits greater post-peak strength loss due to weaker confinement. Additionally, C-G-1-100, which features a simpler tie configuration (Config. 1 in Figure 11), results in lower deformability and reduced post-peak stress compared to the C-G-3 configurations.

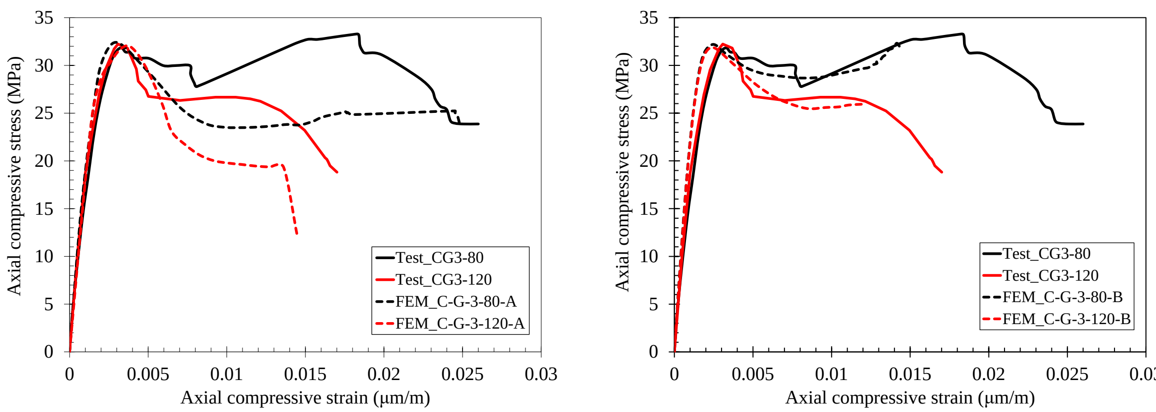

(a) **(b)**

Figure 18 –FEM model performance versus large scale tests [8]: a) Approach A, and b) Approach B

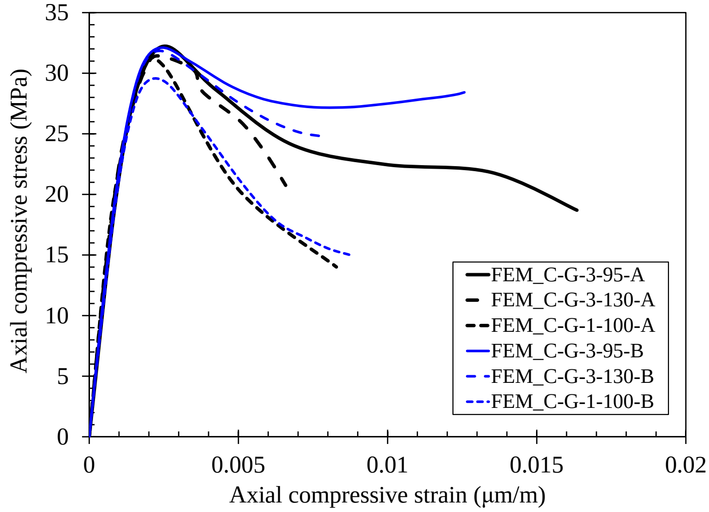

Figure 19 – Axial stress versus strain for the new models using Two modeling approaches

To compare the two finite element modeling approaches, Table 5 highlights key aspects of each method. Approach A employs solid elements for reinforcement with the advanced LaRC05 damage model, while Approach B simplifies the reinforcement modeling using beam elements embedded in concrete.

Table 5 – Summary of advantages and limitations of each FEM approach

Criteria	Approach A	Approach B
Ease of modeling	Complex meshing due to detailed reinforcement	Simple meshing with embedded reinforcement
Computation cost	High computational demand, requiring symmetric modeling	Lower computational cost, efficient for large models
Prediction accuracy	Accurate up to peak load and the failure point but underpredicts post-peak load	Captures post-peak load drop more effectively
Prediction of post-peak deformation	More in line with test results	Less in line with test results
Failure recognition in reinforcement	Based on advanced LaRC05 damage model	Must be determined based on stress thresholds
Prediction of failure modes in reinforcement	Matrix cracking, fiber tensile failure, fiber kinking, and fiber splitting	Unavailable
Bond-slip consideration	Explicitly modeled through cohesive interactions	Cannot be directly incorporated
Mesh dependency for reinforcement	Requires fine mesh for reinforcement details	Less sensitive to mesh refinement
Stress transfer mechanism	Captures localized stress transfer in reinforcement	Assumes perfect bond, affecting stress distribution
Reinforcement Damage Modeling	Includes progressive damage and fracture	Requires manual removal of failed elements based on stress limits
Confinement effects	More explicitly captured due to reinforcement-concrete interaction	Less explicit due to embedding assumption
Application for large models	Less feasible due to meshing and computational limits	More feasible for large-scale simulations

Based on table 5 and the observations from Figure 18, a combination of two approaches was used. Approach A for the peak load and before that plus the failure point in the post peak, while approach B for the drop after peak load and the load level that model maintain after drop.

The deformability index for the FEM models was calculated and is presented in Figure 20 alongside the test results. The squares represent the test data, while the crosses indicate the FEM results. The deformability index increases with the transverse reinforcement ratio, and this trend is consistent in both FEM results and experimental data. This demonstrates that the FEM models can accurately capture the relationship between transverse reinforcement and deformability.

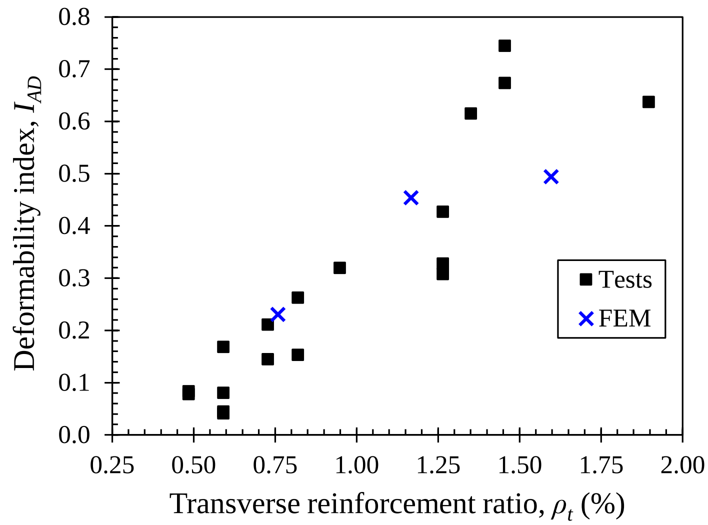

Figure 20 – Experimental results and FEM predictions of I_{AD} versus ρ_t(%)

6. CONCLUSION

In this study focused on the influence of transverse reinforcement configurations on strength, deformability, and post-peak performance of GFRP-RC columns. An experimental method, supported by validated 3D finite element models, allowed for detailed observation of failure modes and stress-strain behavior. The findings highlighted the critical role of tie spacing, overlap lengths, and fastening methods in enhancing ductility and preventing premature failure.

Based on stress-strain or axial load-displacement diagrams from studies on large-scale columns in the literature, a new deformability index is proposed. The calibrated FEM, along with another commonly used FEM approach, was utilized for further validation.

The following are the main conclusions:

<u>New small-scale tests and FEM:</u>

- Since the concrete cover has a negligible effect on the post-peak behavior of the columns, a new testing approach was introduced in which small-scale columns were cast without a concrete cover using a specialized forming method. This allowed for direct observation of the failure mechanisms of GFRP bars and ties during testing. The comparison between experimental results and 3D FE models, which account for damage in bars, ties, and concrete, showed strong agreement, particularly in capturing the failure modes and post-peak behavior of small-scale columns.
- In specimens with a tie spacing of 100 mm (around $6d_b$), the FE models predicted failure at peak loads of approximately 30 MPa, closely matching the experimental results. The models also accurately reflected the increased confinement and higher second peak loads (up to 25 MPa) in specimens with longer tie overlap lengths ($28d_t$).
- Columns with 200 mm tie spacing (around $12d_b$) demonstrated reduced confinement, leading to earlier failure and more pronounced cracking. The FE model showed a significant drop in stress after reaching a maximum of around 23 MPa, aligning with the test results where the absence of ties in the central region led to buckling of longitudinal bars, insufficient confinement and rapid post-peak degradation.

<u>Tie spacing and fasteners intervals:</u>

- It was observed that $6d_b$ tie spacing promotes ductility and even the emergence of a second peak in load capacity under large strains as observed in this study and literature. For continuous tie configurations (C-shape), maintaining a maximum tie spacing of $6d_b$ is essential to ensure deformability and structural integrity.
- Specimens with a $28d_t$ tie overlap and a $12d_b$ length of 90° hooks demonstrated improved structural integrity, allowing the ties to remain functional beyond the first peak load. The introduction of zip ties at $3d_t$ intervals provided sufficient confinement to enhance deformability, as observed in the experimental results.
- Increasing the tie overlap length from $20d_t$ to $28d_t$ improved confinement, delaying bar buckling and increasing second peak load by 17%.
- Reducing the tie spacing from $12d_b$ to $6d_b$ increased the deformability index from 0.25 to 0.8 and enhanced post-peak load retention from 0.001 μm/m to 0.011 μm/m.

<u>Deformability index and large-scale FEM:</u>

- By studying the shape of the stress-strain or load-displacement curves at post-peak form tests in literature a ductility index was proposed for reinforced columns with GFRP bars and ties having a linear relationship with the transverse reinforcement ratio (not volumetric). Three deformability index levels (high, moderate, and minimum) were determined based on the three distinct categories of axial load-displacement or axial stress-strain behavior observed.
- Two FEM approaches were compared for large-scale columns. Approach A uses solid elements with the LaRC05 damage model, capturing reinforcement failure and confinement effects but at a high computational cost and with post-peak underprediction. Approach B, with embedded beam elements, is more efficient and better matches post-

peak behavior but assumes perfect bond and lacks explicit reinforcement failure modeling. The choice depends on the trade-off between accuracy and computational efficiency.

- It is suggested that future research explores larger column sizes and different tie diameters to assess their behavior more comprehensively. Additionally, variations in material properties (modulus and strength) and the spacing of fasteners should be further investigated to enhance the understanding of their effects on structural performance.

CRediT authorship contribution statement

Alireza Sadat Hosseini: Conceptualization, Investigation, Data Curation, Methodology, Visualization, Writing - original draft. **Pedram Sadeghian**: Funding acquisition, Project administration, Resources, Writing - review & editing, Supervision.

REFERENCES

[1] H. Jawaheri Zadeh and A. Nanni, "Design of RC columns using glass FRP reinforcement," *Journal of Composites for Construction*, vol. 17, no. 3, pp. 294–304, 2013.

[2] ACI, *ACI-318-11: Building Code Requirements for Structural Concrete and Commentary*. American Concrete Institute, 2011.

[3] A. De Luca, F. Matta, and A. Nanni, "Behavior of full-scale glass fiber-reinforced polymer reinforced concrete columns under axial load," *ACI Struct J*, vol. 107, no. 5, p. 589, 2010.

[4] M. Elchalakani and G. Ma, "Tests of glass fibre reinforced polymer rectangular concrete columns subjected to concentric and eccentric axial loading," *Eng Struct*, vol. 151, pp. 93–104, 2017.

[5] M. Guérin, H. M. Mohamed, B. Benmokrane, C. K. Shield, and A. Nanni, "Effect of Glass Fiber-Reinforced Polymer Reinforcement Ratio on Axial-Flexural Strength of Reinforced Concrete Columns.," *ACI Struct J*, vol. 115, no. 4, 2018.

[6] M. Guérin, H. M. Mohamed, B. Benmokrane, A. Nanni, and C. K. Shield, "Eccentric Behavior of Full-Scale Reinforced Concrete Columns with Glass Fiber-Reinforced Polymer Bars and Ties.," *ACI Struct J*, vol. 115, no. 2, 2018.

[7] ACI, *ACI-318-14: Building Code Requirements for Structural Concrete and Commentary*. American Concrete Institute, 2014.

[8] H. Tobbi, A. S. Farghaly, and B. Benmokrane, "Concrete Columns Reinforced Longitudinally and Transversally with Glass Fiber-Reinforced Polymer Bars.," *ACI Struct J*, vol. 109, no. 4, 2012.

[9] H. Tobbi, A. S. Farghaly, and B. Benmokrane, “Behavior of Concentrically Loaded Fiber-Reinforced Polymer Reinforced Concrete Columns with Varying Reinforcement Types and Ratios.,” *ACI Struct J*, vol. 111, no. 2, 2014.

[10] H. Tobbi, A. S. Farghaly, and B. Benmokrane, “Strength model for concrete columns reinforced with fiber-reinforced polymer bars and ties,” *ACI Struct J*, vol. 111, no. 4, pp. 789–798, 2014.

[11] K. Khorramian and P. Sadeghian, “Experimental investigation of short and slender rectangular concrete columns reinforced with GFRP bars under eccentric axial loads,” *Journal of Composites for Construction*, vol. 24, no. 6, p. 04020072, 2020.

[12] A. Salah-Eldin, H. M. Mohamed, and B. Benmokrane, “Effect of GFRP reinforcement ratio on the strength and effective stiffness of high-strength concrete columns: Experimental and analytical study,” *Journal of Composites for Construction*, vol. 24, no. 5, p. 04020055, 2020.

[13] N. Elmesalami, F. Abed, and A. El Refai, “Concrete columns reinforced with GFRP and BFRP bars under concentric and eccentric loads: Experimental testing and analytical investigation,” *Journal of Composites for Construction*, vol. 25, no. 2, p. 04021003, 2021.

[14] M. Z. Afifi, H. M. Mohamed, and B. Benmokrane, “Strength and axial behavior of circular concrete columns reinforced with CFRP bars and spirals,” *Journal of Composites for Construction*, vol. 18, no. 2, p. 04013035, 2014.

[15] H. M. Mohamed, M. Z. Afifi, and B. Benmokrane, “Performance evaluation of concrete columns reinforced longitudinally with FRP bars and confined with FRP hoops and spirals under axial load,” *Journal of Bridge Engineering*, vol. 19, no. 7, p. 04014020, 2014.

[16] H. Karim, B. Noel-Gough, M. N. Sheikh, and M. N. S. Hadi, “Strength and ductility behavior of circular concrete columns reinforced with GFRP bars and helices,” in *The 12th International Symposium on Fiber Reinforced Polymers for Reinforced Concrete Structures (FRPRCS-12)*, 2015.

[17] M. N. S. Hadi, H. Karim, and M. N. Sheikh, “Experimental investigations on circular concrete columns reinforced with GFRP bars and helices under different loading conditions,” *Journal of Composites for Construction*, vol. 20, no. 4, p. 04016009, 2016.

[18] A. Hadhood, H. M. Mohamed, and B. Benmokrane, “Axial load–moment interaction diagram of circular concrete columns reinforced with CFRP bars and spirals: Experimental and theoretical investigations,” *Journal of Composites for Construction*, vol. 21, no. 2, p. 04016092, 2017.

[19] W. Abdelazim, H. M. Mohamed, B. Benmokrane, and M. Z. Afifi, “Effect of critical test parameters on behavior of glass fiber-reinforced polymer-reinforced concrete slender columns under eccentric load,” *ACI Struct J*, vol. 117, no. 4, pp. 127–141, 2020.

[20] M. Elchalakani, M. Dong, A. Karrech, M. S. Mohamed Ali, and J.-S. Huo, “Circular concrete columns and beams reinforced with GFRP bars and spirals under axial, eccentric, and flexural loading,” *Journal of Composites for Construction*, vol. 24, no. 3, p. 04020008, 2020.

[21] M. N. S. Hadi, S. Ali, and M. Neaz Sheikh, “Experimental Study of GFRP-Reinforced Geopolymer Concrete Columns under Different Loading Conditions,” *Journal of Composites for Construction*, vol. 25, no. 6, p. 04021052, 2021.

[22] ACI, *ACI CODE-440.11-22: Building Code Requirements for Structural Concrete Reinforced with Glass Fiber-Reinforced Polymer (GFRP) Bars-Code and Commentary*. American Concrete Institute, 2022.

[23] ACI, *ACI 318-19: Building Code Requirements for Structural Concrete and Commentary*. American Concrete Institute, 2019.

[24] ASTM, *ASTM D7205/D7205M, Standard Test Method for Tensile Properties of Fiber-Reinforced Polymer Matrix Composite Bars*. 2021.

[25] A. Sadat Hosseini and P. Sadeghian, "Assessing Compressive Properties of GFRP Bars: Novel Test Fixture and Statistical Analysis," *Journal of Composites for Construction*, vol. 29, no. 2, p. 04025011, 2025.

[26] B. Fillmore and P. Sadeghian, "Contribution of longitudinal glass fiber-reinforced polymer bars in concrete cylinders under axial compression," *Canadian Journal of Civil Engineering*, vol. 45, no. 6, pp. 458–468, 2018.

[27] K. Khorramian and P. Sadeghian, "New testing method of GFRP bars in compression," in *CSCE Annual Conference 2018, Fredericton, NB, Canada*, Canadian Society for Civil Engineering, 2018.

[28] T. D'Antino and M. A. Pisani, "Tensile and compressive behavior of thermoset and thermoplastic GFRP bars," *Constr Build Mater*, vol. 366, p. 130104, 2023.

[29] A. Sadat Hosseini, S. K. Velkumar, and P. Sadeghian, "Behavior of GFRP-Reinforced Concrete Members under Combined Bending Moment and Low Axial Load," *Journal of Composites for Construction*, vol. 28, no. 4, p. 04024025, 2024.

[30] L. Bujotzek, D. Beck, E. Apostolidi, and D. Waldmann, "Experimental and statistical investigations of the material properties of FRP reinforcement in compression," *Constr Build Mater*, vol. 414, p. 134782, 2024.

[31] Dassault Systèmes SIMULIA Corp., *ABAQUS/CAE Reference Manual*. 2023.

[32] S. T. Pinho, R. Darvizeh, P. Robinson, C. Schuecker, and P. P. Camanho, "Material and structural response of polymer-matrix fibre-reinforced composites," *J Compos Mater*, vol. 46, no. 19–20, pp. 2313–2341, 2012.

[33] S. T. Pinho, C. G. Dávila, P. P. Camanho, L. Iannucci, and P. Robinson, "Failure models and criteria for FRP under in-plane or three-dimensional stress states including shear non-linearity," 2005.

[34] J. Lubliner, J. Oliver, S. Oller, and E. Oñate, "A plastic-damage model for concrete," *Int J Solids Struct*, vol. 25, no. 3, pp. 299–326, 1989, doi: https://doi.org/10.1016/0020-7683(89)90050-4.

[35] J. Lee and G. L. Fenves, "Plastic-damage model for cyclic loading of concrete structures," *J Eng Mech*, vol. 124, no. 8, pp. 892–900, 1998.

[36] J. Lee and G. L. Fenves, "A plastic-damage concrete model for earthquake analysis of dams," *Earthq Eng Struct Dyn*, vol. 27, no. 9, pp. 937–956, 1998.

[37] S. Popovics, “A numerical approach to the complete stress-strain curve of concrete,” *Cem Concr Res*, vol. 3, no. 5, pp. 583–599, 1973.

[38] A. S. Genikomsou and M. A. Polak, “Finite element analysis of punching shear of concrete slabs using damaged plasticity model in ABAQUS,” *Eng Struct*, vol. 98, pp. 38–48, 2015.

[39] A. Hillerborg, M. Modéer, and P.-E. Petersson, “Analysis of crack formation and crack growth in concrete by means of fracture mechanics and finite elements,” *Cem Concr Res*, vol. 6, no. 6, pp. 773–781, 1976.

[40] H. Behnam, J. S. Kuang, and B. Samali, “Parametric finite element analysis of RC wide beam-column connections,” *Comput Struct*, vol. 205, pp. 28–44, 2018.

[41] M. Hafezolghorani, F. Hejazi, R. Vaghei, M. S. Bin Jaafar, and K. Karimzade, “Simplified damage plasticity model for concrete,” *Structural engineering international*, vol. 27, no. 1, pp. 68–78, 2017.

[42] N. Shakouri Mahmoudabadi *et al.*, “Effects of eccentric loading on performance of concrete columns reinforced with glass fiber-reinforced polymer bars,” *Sci Rep*, vol. 14, no. 1, p. 1890, 2024.

[43] R. S. Spozito *et al.*, “Numerical Modeling of Four-Pile Caps Using the Concrete Damaged Plasticity Model,” *Buildings*, vol. 14, no. 7, p. 2066, 2024.

[44] J. Alves, A. El-Ragaby, and E. El-Salakawy, “Durability of GFRP bars’ bond to concrete under different loading and environmental conditions,” *Journal of composites for construction*, vol. 15, no. 3, pp. 249–262, 2011.

[45] H. Abbas, M. A. Alanazi, H. Elsanadedy, T. Almusallam, A. Abadel, and Y. Al-Salloum, “Effect of tie spacing and GFRP rebar diameter on compression behavior of concrete columns,” *Journal of Building Engineering*, vol. 72, p. 106740, 2023.

[46] M. N. S. Hadi and J. Youssef, “Experimental investigation of GFRP-reinforced and GFRP-encased square concrete specimens under axial and eccentric load, and four-point bending test,” *Journal of Composites for Construction*, vol. 20, no. 5, p. 04016020, 2016.

[47] F. Abed, N. G. Aswad, and K. Obeidat, “Effect of BFRP ties on the axial performance of RC columns reinforced with BFRP and GFRP rebars,” *Compos Struct*, vol. 340, p. 118184, 2024.

[48] G. N. Prajapati, A. S. Farghaly, and B. Benmokrane, “Performance of concrete columns longitudinally reinforced with steel and GFRP bars and confined with GFRP spirals and cross ties under reversed cyclic loading,” *Eng Struct*, vol. 270, p. 114863, 2022.